Magnetic fabrics as strain markers in folded soft-sediment layers

R. Weinberger[1, 2], G.I. Alsop[3], and T. Levi[1]

1) Geological Survey of Israel, Jerusalem, Israel. email: rami.weinberger@gsi.gov.il

2) Department of Geological and Environmental Sciences, Ben Gurion University of the Negev, Beer Sheva, Israel.

3) Department of Geology and Geophysics, School of Geosciences, University of Aberdeen, Aberdeen, UK.

Abstract

We exploit the potential of magnetic fabrics acting as strain markers in folded layers, by analysing an exceptionally well-exposed, recent (<1 kyr) slump horizon in unlithified lake deposits within the Dead Sea basin. The ~3-m-long folded soft-sediment layer, together with an underlying basal detachment, and an 'undeformed' reference layer are extensively sampled (n=97) for an anisotropy of magnetic susceptibility (AMS) analysis. This analysis reveals deformation fabrics within the folded layer which are significantly different from fabrics detected in the 'undeformed' layer. The maximum magnetic susceptibility axes (K_1) show a hinge-parallel orientation, and the minimum magnetic susceptibility axes (K_3) show a trail of orientations directed eastward parallel to the direction of downslope slumping toward the depocenter of the basin. In terms of shape of the AMS, samples from the 'undeformed' layer are oblate, while the majority of samples from the fold backlimb are oblate to neutral, and those from the forelimb and hinge zones are more prolate. We postulate that the deformation shown by the AMS analysis approximates well to sections through the strain

ellipsoid in the folded layer, suggesting that magnetic fabrics serve as strain markers that are invisible to the naked eye. The deformation fabrics are created by particles moving relative to one another and reorganising during hydroplastic deformation. Particles physically rotate in the hinge zone, resulting in shortening of the intermediate axes and creation of more prolate shapes. The combination of two types of fabrics (deposition and deformation) in the hinge zones increases the intensity of the lineation due to the intersection of the primary and secondary fabrics (foliations). Based on the dense sampling scheme, we produce GIS-based interpolation maps that show the spatial distribution of the AMS parameters in the folded layer. These maps are compared to data from classical strain analyses, providing a benchmark for combining traditional structural methods and AMS analyses in studying folding and soft-sediment deformation.

1. Introduction

Folds are one of the most abundant and widespread structures on Earth, ranging in scale from sub-mm to many km and preserving valuable information about the deformation history of both rocks and sediments. Modern fold theory and techniques developed by John Ramsay (Ramsay, 1967) and co-workers (e.g., Ramsay and Huber, 1983, 1987; Ramsay and Lisle, 2000) have greatly improved our ability to describe the geometry of the folds, analyse fold kinematics and infer the mechanisms of their origin. One of the great challenges in these analyses is to gain a 3D view of the accumulated strain by combining 2D data from several differently oriented sections (Fossen, 2016). To this end, the potential of magnetic fabrics, mainly anisotropy of magnetic susceptibility (AMS) fabrics, have been exploited as a proxy to strain (e.g., Hrouda, 1982; Borradaile and Jackson 2010 and reference therein). The basis of relating AMS fabrics and strain is rooted in the mathematics of these quantities, which are both second-rank tensors that describe the anisotropic physical property and state of the material, respectively. The maximum K_1, intermediate K_2 and minimum K_3 magnetic susceptibility axes (eigenvectors) correspond to k_1, k_2 and k_3 eigenvalues of the AMS. The eigenvectors and eigenvalues define the orientation and shape of the AMS ellipsoid, in much the same way as the directions of the principal strain axes (X≥Y≥Z) and their magnitudes define the orientation and shape of the strain ellipsoid (Borradaile, 2003). In sediments and sedimentary rocks, the K_1 and K_3 axes are generally parallel to the long and short axes of grain shapes, respectively. For platy particles such as clay, K_3 axes are typically parallel to the short axes of the particle shapes (Borradile and Henry, 1997). When deposited in still-water, elongate and platy particles tend to lie parallel to the horizontal bedding plane, forming a 'deposition fabric'. In this fabric, the K_1 and K_2 axes lie within the bedding plane and are indistinguishable, while the K_3 axes are vertical and well-clustered, forming an oblate shape to the AMS ellipsoid ($k_3 << k_1, k_2$). In a fluvial-lacustrine environment that enhances weak particle alignment (Rees, 1983), a 'quasi-deposition fabric' evolves in which the oblateness of the AMS ellipsoid is quite strong but K_1 and K_2 axes are well-clustered and distinguishable (Levi et al., 2006a). During later soft-sediment deformation (Maltman, 1984), the original fabric might evolve into a 'deformation fabric', in which the K_1 and K_2 axes are well-clustered and distinguishable and the shape of the AMS ellipsoid changes gradually from oblate ($k_3 << k_1, k_2$) to prolate ($k_3, k_2 << k_1$).

In many deformed environments, the principal AMS axes (eigenvectors) are coaxial with the directions of the principal strain axes (Borradaile 1988, 1991; Averbuch et al., 1992; Borradaile and Henry, 1997; Mattei et al., 1997; Mattei et al., 1999; Parés et al., 1999; Hirt et al., 2000; Cifelli et al., 2004; Cifelli et al., 2005; Soto et al., 2009; Borradaile and Jackson, 2010; Mamtani et al., 2013; Mamtani et al., 2017). Although there has been limited success in the scaling between the AMS eigenvalues and the strain magnitudes, the overall shape of the AMS ellipsoid (e.g., oblate versus prolate) provides a fair to good approximation of the strain geometry of the deformed rocks and sediments (e.g., Hrouda, 1993; Borradaile and Jackson 2010). In that regard, the spatial distribution of magnetic fabrics in folded lithified rocks (e.g., granitoids, quartzites) were previously studied and variations in the degrees of anisotropy in the various structural domains (fold limbs, hinges) were derived (Mukherji et al., 2004; Mamtani and Sengupta, 2010). However, these AMS-structural relations have scarcely been tested for folded layers in unlithified, soft-sediment which form the focus of the present study.

In previous works, we studied the magnetic fabrics of the late-Pleistocene Lisan Formation, facilitating comparison between directions of AMS axes and the transport directions of slump horizons within the Dead Sea basin (Weinberger et al., 2017). We applied AMS to characterize various seismites, including injected clastic dykes (Levi et al., 2006a; Levi et al., 2006b), breccia layers (Levi et al., 2018), fold-thrust systems (Alsop et al., 2020a), bedding-plane slips (Weinberger et al., 2016) and co-seismic fault zones (Levi et al., 2014; Elhanati et al., 2020) that have been triggered by earthquakes along the seismically-active Dead Sea Fault (Garfunkel, 1981). In this work, we further investigate the potential of magnetic fabrics as strain markers, expediting the interpretation of fold kinematics during soft-sediment deformation. We take advantage of the exceptionally well-exposed, recent (<1 kyr) slump horizons in lake deposits within the Dead Sea basin. The advantage of this setting compared to folds in lithified rocks which may have identical geometries (e.g. Hudleston, 1986; Alsop et al., 2019) is that laminated lake sediments provide detailed and precise markers of fold shapes, which are largely unaffected by subsequent processes. These sediments are exposed due to continuous lake-level drop and shrinkage of the Dead Sea, which reveals primary folds that formed in single events due to gravity-driven slumping. The spatial distribution of the magnetic fabrics in a folded layer are compared to Ramsay's (1967) and Lisle's (1992) strain analyses, providing a benchmark for combining traditional and AMS techniques in the study of soft-sediment deformation.

2. Geologic setting

The Dead Sea basin is a pull-apart structure developed between two left-stepping strands of the Dead Sea Fault (DSF) system (Fig. 1a,b; Quennell, 1956; Garfunkel, 1981). The basin is accompanied by a series of oblique-normal faults that juxtapose Cretaceous carbonate rocks against Quaternary lacustrine and alluvial sediments along the basin's western margin fault zone (Fig. 1b, c). The Dead Sea is a terminal lake, the youngest of a series of lakes that have occupied the basin since the Upper Miocene. Late Pleistocene and Holocene fan-deltas are common deposits along the western margins of the Dead Sea (e.g., Sneh, 1979), one of which is the Ze'elim fan-delta that emanates from the Ze'elim Wadi (Fig. 1b, c). Below ca.- 390 m mean sea level (m.s.l.), the Ze'elim fan-delta is dominated by mudflats consisting of 20–40 m of alternating layers of chemical and detrital laminae as well as clay, silt, sand, salt, and gravel of the Holocene Ze'elim Formation, with a ~10 ka salt layer at its base (Yechieli et al., 1993; Ken-Tor et al., 2001). It is currently exposed around the margins of the Dead Sea (Fig. 1b) and has also been recovered in drill cores taken from nearer the depocentre of the basin (Lu et al., 2017; Kagan et al., 2018). The shore-margin strip at the western edge of the basin displays a ~5° slope, which steepens to 20° below the present water level (Coianiz et al., 2019). This area was first exposed during the late 1970's in response to a drop in the Dead Sea water level and is currently undergoing rapid gully incision as ~1 m per year falls in water levels continue (Avni et al., 2016).

The Ze'elim Formation records deformation such as seismites and injection structures, which were associated with earthquakes related to the DSF (Enzel et al., 2000; Ken-Tor et al., 2001;

Kagan et al., 2011). Slump horizons and mass transport deposits (MTD) are abundant in shore-margin strip (Alsop and Weinberger, 2020). In a previous study on the Ze'elim Formation in the fan-delta (Fig. 1), Alsop and Weinberger (2020a) analysed the variation in fold geometry and orientations down the length of an individual 'creeping' slump at the Ze'elim gully. Fold hinges define broad arcs at high angles to flow in the downslope toe of the slump and progressively swing to become sub-parallel to flow in the upslope region. The swing in trends of fold hinges and axial planes is a consequence of differential layer-normal shear rather than downslope strain gradients (Alsop and Weinberger, 2020).

In this study, we focus on soft-sediment deformation and slump horizons located in the northernmost part of the fan in the Ze'elim gully (GPS coordinates: 31.352296N 35.415178E; Fig. 1c). The studied slump profile sits directly beneath modern gravels that form the Ze'elim fan-delta, indicating that the section forms the very youngest part of the Ze'elim Formation. Structural data collection and AMS sampling were performed along a WSW-ENE trending wall of the gully (Fig. 2a), which provides an almost prefect profile-view of the slump horizon. The slump studied by Alsop and Weinberger (2020) is located several tens of meters upstream along the same gully.

In the lacustrine sediments of the Dead Sea basin, the light-coloured laminae are needles of aragonite of chemical origin forming a diamagnetic phase, and the dark-coloured detrital laminae are platy clays of fluvial-aeolian origin forming the paramagnetic phase (Levi et al., 2006b; Elhanati et al., 2020; Ebert et al., 2020). The ferromagnetic (s.l) particles in the detrital laminae are mainly titanomagnetite, which are transported to the lake by fluvial and aeolian systems, and greigite, which is a diagenetic product of microbial sulphate reduction activity in the lake (Ron et al., 2006; Frank et al., 2007; Ebert et al., 2020).

3. Methods and sampling strategy

3.1. General

The studied slump horizon consists of a ~3-m-long folded layer with nine anticline-syncline fold pairs that collectively form a 'fold train', with individual inflection lines dividing adjacent structures that are denoted (from west to east) as F_1, F_2, …., F_9 (Fig. 2). An anticline typically consists of a long, thin backlimb and a short, thick and inverted forelimb that are separated by an axial plane (Fig. 2). F_6 and F_7 have a somewhat different geometry that resembles a 'box-fold' or 'double-vergence' fold. Due to the size of AMS specimens compared to the folds, it is useful to define anticline and syncline hinge zones, which extend into the zone of maximum curvature on both sides of the associated axial planes.

3.2. Structural analyses

3.2.1. Dip-isogon method and thickness variables

The dip-isogon method is a well-established technique of fold classification, where dip isogons join points of equal dip on adjacent folded surfaces within the fold profile (Ramsay 1967, p.363). In this analysis, t_0 is layer thickness measured along the axial plane, while t_α is orthogonal layer thickness measured at various angles to the reference plane orientated at 90° to the axial plane. Graphs normalise thicknesses by using t'_α (where $t'_\alpha = t_\alpha / t_0$) and plot this value against dip angle (α) to create a series of fold classes (Fig. 3; Ramsay 1967, p. 366). Class 1 folds are marked by convergent dip isogons, Class 2 folds by parallel dip isogons, and Class 3 folds by diverging dip isogons (e.g., Fossen 2016, p.263). In the present study, the dip-isogon method was used to analyse and compare fold geometries formed in a detrital-rich (brown) marker bed (Fig. 3). Our analysis includes dip isogons from both the backlimb and forelimbs of the hinge zones.

3.2.2. Measuring fold parameters and strain contour maps

There are a range of parameters that may be measured on folds to investigate and compare their geometries. Amplitude (A) is defined as half the distance from the trough to the crest of upright folds. Wavelength (λ) is defined as the distance between two points that occupy a similar position on the fold train (i.e. between adjacent anticline hinges). Wavelength may also be measured as double the horizontal distance between neighbouring fold hinges, i.e. double the distance between anticline and syncline fold hinges, forming a fold pair (Schmalholz and Podladchikov, 2001, p. 206). Thickness of a layer (h) is measured orthogonal to the folded layer, and can be taken on the backlimb, forelimb or along the axial plane (AP) of the fold. We analyse folds by comparing amplitudes, wavelengths and layer thicknesses from different positions on the folds together with the AMS analysis. For each fold, we also calculate the backlimb to forelimb thickness ratio (R_{BF}), the forelimb to backlimb thickness ratio (R_{FB}), and the forelimb to axial-plane thickness ratio (R_{FAP}).

Strain contour maps estimate the strain and viscosity contrast between layers during folding and are calculated by measuring amplitude (A), layer thickness (h), and wavelength (λ) in the profile plane of single layer folds (e.g. Schmalholz and Podladchikov, 2001; see also Hudleston and Treagus, 2010). The strain contour map compares amplitude / wavelength (A/λ) and layer thickness / wavelength (h/λ), with estimates of bulk strain (in terms of % shortening) and the layer / matrix viscosity ratio being made by reading the position of data directly off the map (Schmalholz and Podladchikov 2001). The technique assumes linear viscous folding rather than power law viscous folding and involves analysis of single layer folds (i.e. unaffected by neighbouring competent beds) (Schmalholtz and Podladchikov

2001). The technique also presumes all the layer shortening is taken up by buckling with no out-of-plane movement and was previously applied to soft-sediment folds by Alsop et al. (2020b).

3.2.3. Inverse-thickness method

The inverse-thickness method was introduced by Lisle (1992) and calculates the post-buckling flattening strain of folds. Assuming that the folds have a parallel (Class 1B) shape before flattening, the stretch of the layer at any position in the flattened fold is inversely proportional to the orthogonal thickness of the layer. A polar graph showing inverse thickness as a function of layer orientation (i.e., tangent orientation) directly yields the shape and orientation of the flattening strain ellipse. The *Rs* value defines the ratio of the long to short axes of the strain ellipse and were visually fitted through the points on the inverse thickness graph (Fig. 4).

3.3. AMS analysis

3.3.1. Sampling and measurements

Oriented samples were collected from the Ze’elim sediments using 25 × 20 mm (length x diameter) Perspex (Polymethyl methacrylate) cylinders, which have negligible diamagnetic susceptibility. In total 97 samples were collected, with 58 from the folded slump horizon, 19 from the basal detachment, 10 from the toe of the slump, and 10 from an ‘undeformed’ reference layer located 500 m upstream along the Ze’elim gully. Practically, the samples from the basal detachment include a ~25 mm-thick layer that corresponds to the diameter of the Perspex cylinders, each of which contains several sheared laminae and adjacent, less deformed laminae. Samples were sequentially numbered from west to east along the folded slump horizon, and samples were further categorized into their structural domains. First, samples from the anticlinal and synclinal hinge zones were categorized, and then the rest of the samples were grouped into backlimb and forelimb domains. Because the backlimbs are much longer than the forelimbs, the number of samples taken from backlimbs is five times more than from forelimbs. The AMS was measured at the Geological Survey of Israel rock-magnetic laboratory, using a *KLY-5* Kappabridge (AGICO Inc.) following the procedures described in Issachar et al. (2019b). The rock magnetic characterizations of the lacustrine sediments of the Dead Sea basin were intensively studied in previous works and are not repeated here (e.g. Ron et al., 2006; Levi et al., 2006a, 2006b; Frank et al., 2006; Ebert et al., 2020; and Elhanati et al., 2020).

3.3.2. AMS parameters and their spatial distribution

The AMS was analysed with *Anisoft4.2* and the mean susceptibility $k_m = (k_1 + k_2 + k_3)/3$, magnetic lineation ($L= k_1/k_2$), magnetic foliation ($F= k_2/k_3$), degree of anisotropy or eccentricity ($P= k_1/k_3$) and the shape of the AMS ellipsoid ($T= 2\ln(k_2/k_3)/\ln(k_1/k_3)-1$) were calculated according to Jelínek (1981) and Tarling and Hrouda (1993). These AMS parameters were analysed using Geographical Information System (GIS), constructing interpolated maps that show the spatial distribution of *L, F, P, T,* and *L*/*F* in the folded layer. The GIS-based maps help to characterize different domains of deformation along the folded layer and compare them with structural data, including values of *Rs* and R_{BF}. First, the boundaries of the folded layer and the locations of the samples were digitized and the values of the AMS parameters were tabulated. Next, values of the AMS parameters were interpolated by the Inverse Distance Weighted tool (IDW) and the GIS-based spatial distribution maps were produced.

4. Results

4.1. Structural data

The slump horizon is detached along a basal surface that dips ~5º eastward towards the Dead Sea basin, forming a series of fold pairs that verge towards ~E (i.e.. axial planes dip toward ~W). Fold hinges are sub-horizontal and trend N to NNE- (Fig. 2: inset) with a mean plunge and trend orientation of 05º/013º and α_{95}=10º. The synclines are typically mirror symmetries of the anticlines (Fig. 2). Short thrusts with a few cm of displacement that decreases upwards branch from the basal detachment, forming a 'mini fold and thrust system' just above it.

The isogon patterns of most folds are almost parallel and consistent with Class 2 similar folds (Fig. 3). In detail, isogons of F_1 are slightly divergent (Class 1C) (Fig. 3c) and those of F_3 and F_5 are slightly convergent (Class 3) (Fig. 3j,k). Differences in the isogon and thickness patterns between the backlimb and forelimb parts of the hinge zones are generally minor, with the forelimb being somewhat more of a Class 2 fold (e.g., Fig. 3j). The 'double-vergence' folds show mainly a Class 1B pattern for the backlimb of F_6 and the forelimb of F_7 (Fig. 3k). Flattening of folds is distinct with values of *Rs* between 1.92 and 4.08. The upper value is associated with F_8, which has a sub-horizontal axial plane and recumbent geometry, whereas the lower value is related to F_6 with a more upright axial plane (Fig. 4).

Values of R_{FB} are between 0.8 and 3.4 with the higher values being associated with F_8 and F_3 (Fig. 5). Values of forelimb to axial-plane thickness ratio R_{FAP} versus elliptical ratio *Rs* are presented in Fig. 5d, and show that increased forelimb thickness corresponds to lower *Rs*. Within the fold train, amplitude of folds (*A*) increases as the wavelength (λ) reduces, so that the A/λ ratio defines a general trend when plotted against λ (Fig. 5a, b). However, the A/λ ratio is not a straight line when compared to wavelength, with wavelength increasing proportionally more than amplitude (Fig. 5b). Analysis of individual fold data on the strain contour map of Schmalholz and Podladchikov (2001) suggests that the folded layer displays viscosity contrasts in a typical range between 50 and 250, while calculated layer shortening is less than 60%, (Fig. 5c). Greater estimates of % shortening (>30%) are associated with the central area of more upright folding (F_3, F_4, F_5). Although considerable scatter exists, especially where A/λ forms smaller ratios, folds with lower % shortening have greater viscosity contrasts compared to adjacent folds with higher % shortening, resulting in more 'gentle' trends than the established lines marking fixed viscosity contrasts on the strain contour map (Fig. 5c).

The inverse-thickness method of Lisle (1992) creates best-fit elliptical ratios (*Rs*) that represent the post-buckling flatting strain of folds (Figs. 4, 5d). The *Rs* value is compared with the forelimb / axial plane thickness ratio (R_{FAP}) of the folded layer and shows that a relative increase in forelimb thickness corresponds to lower *Rs* ratios (Figs. 5d). The more upright folds in the central part of the fold train (F_4, F_5, F_6, F_7) generally display lower *Rs* values and greater R_{FAP}, indicating that steeper forelimbs are relatively thickened during post-buckle flattening. Conversely, the more recumbent folds (e.g. F_3, F_8) with markedly overturned forelimbs display greater axial plane thickening and lower R_{FAP} values that corresponds to greater *Rs* of ~4 (Figs. 5d).

4.2. AMS fabrics

4.2.1. AMS orientations and shapes

The results of the AMS analysis (n=97) are shown in Figs. 6-11, while the measured AMS parameters are provided in the Supplementary Data. The bulk susceptibility of the layers is positive with values ranging between 50 and 1340 x10^{-6} SI (Fig. 6a) with quite similar mean and median values of 452 x10^{-6} SI and 441 x10^{-6} SI, respectively. The orientations of the principal AMS axes (eigenvectors) from the backlimbs, forelimbs, anticline and syncline hinge zones, basal detachment, toe of slump and the 'undeformed' reference layer are plotted in lower-hemisphere, equal-area projections (Fig. 7). For the same structural domains, the AMS eigenvalues are presented on standard *T-P* plots (Fig. 7).

The 'undeformed' reference layer shows well-clustered, vertical K_3 axes, while K_1 and K_2 axes lie within the bedding plane (girdle) and are distinguishable. The *T-P* plot shows a strong oblate shape with relatively high *P* values, which is indicative of a depositional environment (Parés, 2015). In terms of shape and AMS parameters, this fabric resembles a 'deposition fabric' (i.e.,) but the grouping of K_1 and K_2 indicates that some preferred orientation of particles already occurred during deposition expressed by a 'quasi-deposition fabric'. For the backlimbs, forelimbs and hinge zones, K_3 axes are off-vertical, indicating that these domains were affected by shearing (Weinberger et al., 2017). K_1 axes are sub-horizontal and typically well-clustered in the SSW direction, parallel to the fold hinges (Fig. 7; top-right plot). The *T-P* plots of those domains show significant decrease in the oblateness, changing to very weak oblate up to prolate in the anticline and syncline hinge zones. The fabrics detected in the toe of the slump are different, where K_3 axes are off-vertical and K_1 axes form a high angle to the fold hinges. The shape of the AMS ellipsoid is conspicuously neutral (T~0). The basal detachment shows K_3 axes is off-vertical while K_1 and K_2 axes are distributed along the girdle but are distinguishable. The shape of the AMS ellipsoid varies between strong and weak oblate.

We focus further on the shape of AMS ellipsoids. Diagrams of *T* versus K_m and *P* versus K_m show a poor correlation between the shape and eccentricity of the AMS ellipsoids and the magnetic susceptibility (Fig. 6b, c), indicating that variations in *T* and *P* are not related to mineralogy. We plot the data on a Flinn-type diagram, which compares the intensities of the magnetic lineation versus magnetic foliation (Fig 8a). The AMS ellipsoids from the ‘undeformed’ reference layer are distinctly oblate, showing pronounced ‘flattening’. The AMS ellipsoids from the basal detachment are generally oblate, but show less ‘flattening’ and spread over a wider range of *L*-*F* values than the ‘undeformed’ reference layer. The majority of the backlimb ellipsoids are oblate, with a few showing neutral or slightly prolate, whereas the majority of the forelimb ellipsoids showing pronounced ‘constriction’ and are prolate. Ellipsoids from the hinge zones show a tendency toward prolate, with fabrics from synclinal and anticlinal hinge zones overlapping and largely indistinguishable. Finally, the AMS ellipsoids from the toe of the slump are evenly distributed on both sides of the neutral shape.

Figure 8b shows AMS data plotted in *T*- ln(*L*) diagram (Levi et al., 2018). Similar to the Flinn-type diagram, AMS data are categorized according to their structural domains. Straight trend lines originating in *T*=1 are fitted separately to data obtained from the reference, detachment and folded layers (Fig. 8b). This fitting helps to evaluate if a subset population shares a common value *P* ($P= k_1/k_3$), which represents the degree of anisotropy or eccentricity of the AMS ellipsoid (Levi et al., 2018). Data from the ‘undeformed’ reference layer displays an excellent correlation (R^2=0.96) as do the data from the basal detachment (R^2=0.92). For the folded layer, data from the different structural domains lie closely along the same line/slope for interception at (1,0) but have varied R^2 with data from the forelimbs showing very good correlation (R^2=0.93); data from the backlimbs displaying a fair correlation (R^2=0.70); and data from the anticline and syncline hinge zones showing fair (R^2=0.52) and poor (R^2=0.22) correlations, respectively (Fig. 8b).

Values of the shape parameter *T* are plotted along the studied folded layer and are denoted by a running sample number between 20 (west) and 87 (east) (Fig. 9). Data are differentiated according to their associated fold and structural domains (backlimbs, forelimbs and hinge zones). *T* values fluctuate as the samples move from one domain to another. In several cases, *T* values from the anticline and syncline hinge zones form local 'minima', corresponding to values of $T<0$ and a prolate shape in highly deformed zones. As indicated in the Flinn-type diagram (Fig. 8a), *T* values from the toe of the slump are quite close to $T=0$, corresponding to a neutral shape of the AMS ellipsoid.

The *T* values are plotted against values of R_{FB} (Fig. 5e) and R_{FAP} (Fig. 5f). These plots show that in each case an increase in the relative thickness of the forelimb corresponds to lower *T* values that mark more prolate AMS fabrics. The folds with the lowest *T* value and lower thickness ratios (R_{FB} and R_{FAP}) also generally display a low *Rs* ratio (e.g. F_6) (Fig. 5d, e, f).

4.2.2. Spatial distribution of AMS data

GIS-based maps showing the spatial distribution of *L*, *F*, *P*, *T*, *L*/*F* and *T*/*L* in the folded layer are presented in Figs 10 and 11. Excluding F_1 and F_2, the magnetic lineation is relatively low (i.e., green to yellow colours) in the backlimbs and increases (i.e., gradient of red colour) towards the anticline hinge zones (e.g., F_3, F_8; Fig. 10a). The magnetic foliation is relatively high in the backlimbs, decreasing towards the hinge zones (e.g., F_3, F_8; Fig. 10b). The *P* values within the folded layer are everywhere quite low (relative to the reference), excluding the backlimb of F_8 and the long backlimb of F_1 that might preserve the primary, high value of the 'quasi-depositional fabric' as has commonly been observed in lacustrine sediments (Fig. 7 'undeformed' reference layer; Fig. 10c). The *T* values show the most coherent pattern of all the AMS parameters (Fig. 10d), indicating an oblate shape in the backlimbs and a prolate (or neutral) shape in the hinge zones and forelimbs. The *L*/*F* values display zones of shape variation relative to neutral shape, highlighting the prolate shapes ($L/F>1$) in the hinge zones

(Fig. 11a). The T/L values display pronounced zones of shape variation, also highlighting the prolate shapes in the hinge zones (Fig. 11b).

To facilitate the comparison between the AMS and structural data, values of the long to short axes ratio of the strain ellipse Rs (Fig. 11c) and forelimb to axial-plane thickness ratio R_{FAP} (Fig. 11d) are denoted as single values in the anticline hinge zone of each fold. Representative maps showing Rs and R_{FAP} values on top of the spatial distribution of T and P are presented in Figure 11c, d, e. Many of the hinge zones have 'warm' colours corresponding to low values of T and prolate shapes. A good correlation is observed between the spatial distribution of T and R_{FAP} (presented in inverse colours), corresponding to high deformation and thickness ratios of $R_{FAP} <0.6$. For Rs, a fair affinity to the spatial distribution of T (6 out of 9 values; Fig. 11d) and a weak affinity to the spatial distribution of P (4 out of 9 values; Fig. 11e) within the hinge zones are observed.

5. Discussion

5.1. Fold geometry and kinematics based on structural data

The folded layer is a slump horizon in the late Holocene Ze'elim Formation that formed due to gravity-driven mass transport toward the Dead Sea depocentre. Field observations of adjacent slump horizons indicate that slumping occurs near the surface and the slope failure has been a slow 'creep' event generated by slope instability rather than catastrophic failure associated with large earthquakes (Alsop and Weinberger, 2020). The folded layer consists of a series of regularly-spaced folds, the majority of which are similar (shear; Class 2) folds (Fig. 3). The flattening of the folds as indicated by the inverse-thickness method (Fig. 4) suggests that folding initiated with the formation of regular buckle folds, which progressively changed to more similar-style folds during continuous creep. In this sense, layers became more passive as they flowed and exerted only minor mechanical influence on the folding during the progressive deformation.

In summary, the general correlations between the measured fold wavelengths and amplitudes suggest that the folds initiated by buckling of a relatively competent layer (Fig. 5a, b). The relationships with layer thickness provide broad estimates of viscosity contrasts between layers via strain contour maps (Fig. 5c), while the inverse-thickness method of Lisle (1992) creates best-fit elliptical ratios (*Rs*) that represent the post-buckling flatting strain of folds (Figs. 4, 5d). These plots collectively suggest that buckle folds might be progressively modified by downslope shearing and/or a flattening component of deformation leading to more 'similar' styles of folding.

5.2. AMS fabrics of the folded slump horizon

To gain more insight into the folding process at the microscale, we analyze the magnetic fabrics of the folded layer, which serve as strain markers in the soft-sediments invisible to the naked eye. The poor correlation between the shape $\underline{T}$ and eccentricity P of the AMS ellipsoids and the magnetic susceptibility, allows us to discard the possibility that variations in T and P along the folded layer are related to mineralogy. The AMS analysis aims to approximate the strain geometry but does not intend to estimate the magnitude of the finite strain.

5.2.1. Orientations of the principal AMS axes

Previous studies of slump horizons were mainly focused on the relation between the transport direction of folds in mass transport deposits (MTDs) and the orientation of the principal AMS axes. These studies (Liu et al., 2001; Parés, 2015; Weinberger et al., 2017; Alsop et al., 2020a) show that the AMS fabrics have common affinities to the transport direction including (1) K_1 axes which are oriented parallel to the fold hinges and normal to the axis of the transport direction; (2) K_2 axes which are parallel to the axis of the transport direction; and (3) K_3 axes which deviate from the vertical, showing a trail of axes that are commonly directed toward the absolute transport direction (in a lower hemisphere projection). Based on these affinities, a viable way to infer the transport directions of folds in MTDs and reconstruct the basin depocentre in ancient settings were demonstrated, e.g., inferring the radial pattern of the Lisan slumps toward the depocentre of the Dead Sea Basin (Weinberger et al., 2017). The principal AMS axes of the Ze'elim slumps show similar characteristics to those of the Lisan slumps, including hinge-parallel K_1 axes and a trail of K_3 axes directed eastward toward the depocentre of the basin (Fig. 7). The AMS fabric of the basal detachment shows similarity to the folded layer in which K_1 axes are normal to the shearing direction. This direction of K_1 axes is in agreement with the slow, creeping movement along the basal detachment. In a variety of hydrodynamic settings, K_1 and K_2 axes could switch (Rees, 1983; Levi et al., 2006a, figure 3), including transport along bedding-plane slip surfaces triggered by seismic activity (Weinberger et al., 2016), and flowing along basal surfaces underneath surge glaciers (Hooyer et al., 2008; Raposo et al., 2021).

5.2.2. Shape variations of the AMS ellipsoid

As the general eastward transport direction of the Ze'elim slumps toward the depocentre is well-established by detailed structural measurements (Alsop and Weinberger, 2020) and the trail of K_3 axes (Fig. 7), we further focus on the shape evolution of the AMS fabrics during slumping and folding. The AMS shape of the 'undeformed' reference layer of the Ze'elim sediments has characteristics of the 'quasi deposition fabric', showing a strong oblate AMS ellipsoid and forming a distinct group of data on the Flinn-type diagram, which is characterized by low intensity of magnetic lineation and high intensity of magnetic foliation (Fig. 8a). The deposition environment of the reference layer is also highlighted in the T-P plot (Fig. 7) and the T-ln(L) diagram (Fig. 8b). This fabric is akin to that of the ‘deposition fabric’ of late-Pleistocene Lisan sediments that accumulated in Lake Lisan, the predecessor of the Dead Sea (e.g., Levi et al., 2006a, 2006b, 2014). Notably, even for the ‘undeformed’ reference layer, the shape of the ellipsoid is not purely oblate as T varies between 0.85 and 0.6 (Fig 8b), indicating that the fluvial-lacustrine depositional environment had already enhanced weak particle alignment (Rees, 1983). Nevertheless, the evolved (deformation) fabrics of the slump horizon are significantly different from the pre-slump, primary (quasi-depositional) fabric as discussed below.

Deformation along the basal detachment had already distorted the primary fabric prior to folding, reducing its oblateness and intensity of foliation (Figs. 7, 8). The deformation was localised along a thin set of laminae directly underneath the folded layer, the thickness of which is smaller than the diameter of the obtained AMS samples. At the scale of the samples, the deformed laminae affect the bulk shape of the AMS ellipsoid, separating the samples from the basal detachment from that of the ‘undeformed’ reference layer in the Flinn-type diagram (Fig. 8a). On the T-ln(L) diagram, samples from the undeformed and the detachment layers have a similar origin at T=~0.8 (and a theoretical origin at T=1), but are associated with different lines of constant eccentricity P (Fig. 8b). The slope of each line is inversely related to the values of P, i.e., negative, less steep slope is related to higher values of P (Levi et al., 2018). Hence, the eccentricity of the AMS ellipsoid was reduced during the detachment processes. Since AMS data from the folded layer have the highest negative slope (Fig. 8b), the slumping and folding processes further reduced the ellipsoid eccentricity. Likewise, a general decrease in ellipsoid eccentricity from the initial (depositional) to final (tectonic) conditions were recorded from magnetic fabrics in sandbox models simulating contraction

(Almqvist and Koyi, 2018). The folding changes the fabric from oblate to prolate via a neutral shape (Fig. 9), and increases the intensity of lineation, as is mainly detected in the anticline and syncline hinge zones and also in the intervening, inverted short forelimb (Fig. 10). The AMS data from the toe of the slump extends evenly from both sides of the plane strain line (Figs. 8a, 9), suggesting that they have a neutral fabric that evolves due to the combination of both primary (quasi) deposition fabric and secondary deformation fabric. We present a summary cartoon that illustrates sections through the AMS ellipsoid, corresponding to deformation in different structural domains in a folded soft-sediment layer above a basal detachment (Fig. 12). The cartoon displays schematic Flinn-type diagrams of plotted AMS data, suggesting a gradual transition from a primary oblate shape toward an evolved prolate shape during deformation mainly in the hinge zones and the forelimbs. We postulate that Figure 12 approximates the sections through the strain ellipsoid in a folded layer.

5.3. Rearrangement of particles during folding

The variations in the orientation and shape of the AMS ellipsoids during folding indicates that changes occurred in the soft-sediment down to the microscopic scale. Shearing during slumping would tend to physically rotate particles in such a way that rolling would result in the particle short axes pointing toward the transport direction. The orientation of the particle long axis strongly depends on the hydrodynamic regime together with particle concentration and interaction, and frictional properties of the detachment (Schöfisch et al., 2021), and may point either normal to or parallel to the transport direction (Rees and Woodall, 1975; Rees, 1983). Consequently, the particle short and long axes typically coincide with the direction of the minimum and maximum susceptibility axes, respectively. For the hydrodynamic regime in the lakes formed in the Dead Sea basin, the magnetic fabrics of slump horizons and the basal detachment have a trail of K_3 axes pointing toward the transport direction, and well-clustered K_1 axes parallel to the fold hinges and normal to the transport direction (Weinberger et al., 2017). These changes in the slump horizon are corroborated with changes in the shape of the AMS ellipsoid, as the initial settling of the particles within the bedding plane is distorted. A progressive particle rearrangement occurred in the hinge zones, as particles move toward these zones and rotated into the axial planes of the folds, resulting in a more prolate fabric in the hinge zones and forelimbs than in the backlimbs. This process could be visualized in terms of deformation in metamorphic rocks, keeping in mind the obvious differences between soft-sediment deformation and deformation during metamorphism; i.e., the former process physically rotate and reorient the particles in a hydroplastic process while the latter process changes the crystal orientation via ductile deformation and recrystallisation in the solid state. In that sense, 'S_0' mimics the primary deposition fabric, which are associated with foliation of the original bedding. 'S_1' mimics the folding phase of deformation in the hinge zones, forming foliation parallel to the axial planes. The intersection of 'S_0' and 'S_1' resulted in the formation of lineation 'L_1' in the hinge zones and a prolate shape with its k_1 parallel to the direction of the hinge line. In reality, the magnetic foliation of 'S_0' evolves mainly due to the contribution of the paramagnetic particles, which are platy clays of fluvial-aeolian origin forming the dark detrital laminae (Levi et al., 2006b; Elhanati et al., 2020; Ebert et al., 2020). The magnetic foliation 'S_1' represents those platy clays that rotate into the axial plane at the hinge zones, forming secondary foliation parallel to this plane. The bulk effect is an evolving lineation 'L_1' along the intersection of the primary and secondary fabrics composed of platy clays. Although this effect could spatially be detected in the backlimbs, it is much better developed in the hinge zones (either anticlines or synclines) and forelimbs (Fig. 10), where thickening and deformation are more intense. Our results demonstrate the significant role played by the folding in changing the fabric from depositional to deformation. Layer-parallel shortening may induce small 'invisible' lateral compaction during early stages of slumping, which contributes to particle reorganisation and fabric change (Almqvist and Koyi, 2018).

5.4. AMS fabrics as strain markers

It has long been postulated and affirmed that AMS fabrics serve as subtle strain markers of deformed lithified rocks (e.g., Hrouda, 1982; Tarling and Hrouda, 1993; Borradaile and Jackson, 2010; Levi and Weinberger, 2011; Mamtani et al., 2013; Issachar et al., 2019a; Boiron et al., 2020). We focus on soft-sediment deformation and note that increasing forelimb thickness corresponds to lower *T* values, marking prolate shapes in these zones (Figs. 7, 9). The dense sampling of the folded layer (Fig. 2b) allows us to produce interpolation maps of the AMS parameters and present their spatial distribution. Such maps provide a new avenue for presenting and exploring AMS data and aid in comparisons to traditional structural data. This can be demonstrated by the spatial distribution of *L*/*F* and *T*/*L*, which directly highlights domains that deviate from neutral shape, including hinge zones and forelimbs (Fig. 11a). As the magnetic lineation is parallel to the hinge lines (Fig. 7), the 2D maps approximate a 3D view of the orientation and shape of strain ellipsoids, but provide an imprecise view of their absolute magnitudes. Prolate shapes evolve in the hinge zones parallel to the hinge lines and these zones show pronounced thickening, indicating a good correlation between the shape parameter *T* and the thickness ratio R_{FAP} (Fig. 11c). The flattening of the folds as indicated by values of *Rs* shows a fair correlation to *T* and a weak correlation to *P*, which could be the result of the 3D nature of the folding process (Fig. 11c). The inverse-thickness method provides single values of *Rs* that approximate the strain ellipses in a 2D profile, but particle movements during folding could be out of this (profile) plane. It is notable that sediments acquire relatively high values of *P* during deposition due to particle preferred arrangement within the bedding plane, but commonly display decreasing values of

P during deformation (Fig. 7). This phenomenon explains the weak correlation between *P* and *Rs*. In that sense, the *T* parameter might better approximate the 3D strain geometry of the folded layer and provides an important addition to the traditional 2D methods of obtaining strain geometry. Moreover, obtaining the 3D strain is tedious work that is based on combining 2D data from several differently oriented sections. It is also heavily dependent on pre-existing markers that have changed shape during deformation. Even if strain markers such as conglomerate pebbles exist and can be analysed for 3D strain (Fossen, 2016, p.63-65), they may actually influence folding by serving as sites of hinge nucleation near large, non-spherical stress-concentrating clasts. Our work suggests that magnetic fabrics from folded layers could be of great help in tracing the deformation process by obtaining information about the strain geometry and intensity when classic strain markers are absent, or pose limitations, on the reliability of the analysis.

6. Summary and Conclusions

The study of the folded layer is performed in wet, unlithified sediments of the Holocene Ze'elim Formation, which are only recently exposed due to continuous lake level falls and shrinkage of the Dead Sea. In this situation, the modern slope and the basal detachment are directly visible, slumping having occurred as a single event in the past few centuries, meaning that later tectonics, which might obliterate and complicate the strain path can be discounted. The structural analysis indicates that folding initiated with the formation of regular buckle folds above a basal detachment, which are progressively modified to similar folds during continuous downslope creep. During this process the hinge zones and forelimbs became thicker than the backlimbs.

Greater insight into the folding process at the microscale is gained by analyzing the AMS fabrics of the undeformed and deformed sediments. Within the folded layer, the AMS shows deformation fabrics, which are different from the quasi-deposition fabrics detected in the 'undeformed' reference layers. In terms of orientation, the principal AMS axes in the folded layer show hinge-parallel K_1 axes and a trail of K_3 axes directed eastward toward the depocentre of the Dead Sea basin. In terms of shape, undeformed layers are oblate, whereas the majority of the backlimb data are less oblate, with a few showing neutral or slightly prolate shapes. The majority of data from the forelimb and hinge zones are more prolate. Samples from the toe of the slump have a neutral shape that might evolve due to the combination of both primary (quasi) deposition fabric and secondary deformation fabric. We postulate that deformation recorded by the AMS analysis approximates well to sections through the strain ellipsoid in the folded layer, and serves as strain markers that are invisible to the naked eye. In undeformed layers, clay particles are all flattened and give an oblate shape. The deformation fabrics are created by grains reorganising and particles moving relative to one another. In the hinge zones, particles physically rotate as they enter into the shear zone, resulting in shortening of the intermediate axis and evolving into a prolate shape. Because the hinge zones are thicker than other structural domains, there are more clay particles that rotate and this enhances the evolving prolate shape. The intersection of the primary (deposition) and secondary (deformation) fabrics in the hinge zones increases the intensity of the lineation in these zones relative to its intensity in the backlimbs.

The interpolation maps showing the spatial distribution of the AMS parameters provide a new avenue for presenting and exploring AMS data and comparing them with more classical structural data and techniques developed by John Ramsay amongst others. There is a good correlation between the shape parameter T and the forelimb to axial plane thickness ratio R_{FAP} and a fair correlation to the elliptical Rs ratios. The eccentricity parameter P shows only a weak correlation to the strain variable *Rs* and is less useful as a strain marker. Our study suggests that magnetic fabrics from folded soft-sediment layers could be of great help in tracing the deformation process by obtaining information about the strain geometry and relative intensities when classic strain markers are absent, or pose limitation, on the reliability of the analysis.

Acknowledgements

This study was supported by the Israel Science Foundation (ISF grants 868/17) and a grant from the Israeli Government under Geological Survey of Israel DS project 40706. We thank Catalina Luneburg and Stephen Laubach for efficient editorial handling, together with Ruth Soto and Manish A. Mamtani for helpful reviews and constructive comments. RW was inspired by John Ramsay while participating in a fieldtrip to the Alps led by John in 2002. GIA would like to take this opportunity to acknowledge John Ramsay's support while a post-doc at ETH Zurich in the late 1980's. TL had the privilege of showing John Ramsay outcrops of slump horizons and seismites in the lacustrine sediments of the Dead Sea region during John's visit to Israel in 2008.

References

Almqvist, B. S., Koyi, H. 2018. Bulk strain in orogenic wedges based on insights from magnetic fabrics in sandbox models. Geology, 46(6), 483-486.

Alsop, G.I., Weinberger, R., Marco, S., Levi, T., 2019. Identifying soft-sediment deformation in rocks. J. Struct. Geol. 125, 248–255.

Alsop, G. I., Weinberger, R., 2020. Are slump folds reliable indicators of downslope flow in recent mass transport deposits? J. Struct. Geol., 135, 104037.

Alsop, G.I., Weinberger, R., Marco, S., Levi, T., 2020a. Distinguishing coeval patterns of contraction and collapse around flow lobes in mass transport deposits. J. Struct. Geol. 134, 104013.

Alsop, G.I., Weinberger, R., Marco, S., Levi, T., 2020b. Folding during soft-sediment deformation. In: Bond, C.E., Lebit, H.D. (Eds.), Folding and Fracturing of Rocks: 50 Years Since the Seminal Text Book of J.G. Ramsay, vol. 487. Geological Society Special Publication, pp. 81–104. https://doi.org/10.1144/SP487.1.

Averbuch, O., de Lamotte, D. F., Kissel, C. 1992. Magnetic fabric as a structural indicator of the deformation path within a fold-thrust structure: A test case from the Corbières (NE Pyrenees, France), J. Struct. Geol., 14(4), 461–474.

Boiron, T., Aubourg, C., Grignard, P. A., Callot, J. P. (2020). The clay fabric of shales is a strain gauge. J. Struct. Geol., 104130.

Borradaile, G.J., 1988. Magnetic-susceptibility, petrofabrics and strain. Tectonophysics 156, 1–20. https://doi.org/10.1016/0040-1951(88)90279-x.

Borradaile, G.J., 1991. Correlation of strain with anisotropy of magnetic susceptibility (AMS). Pure Appl. Geophys. 135, 15–29. https://doi.org/10.1007/bf00877006.

Borradaile, G. J., 2003. Statistics of Earth Science Data: Their distribution in time, space and orientation. Springer Science & Business Media. 351p.

Borradaile, G.J., Henry, B., 1997. Tectonic applications of magnetic susceptibility and its anisotropy. Earth-Sci. Rev. 42, 49–93. https://doi.org/10.1016/S0012-8252(96) 00044-X.

Borradaile, G.J., Jackson, M., 2004. Anisotropy of magnetic susceptibility (AMS): magnetic petrofabrics of deformed rocks. Geol. Soc. London, Spec. Publ. 238, 299–360. https://doi.org/10.1144/GSL.SP.2004.238.01.18.

Casas-Sainz, A.M., Gil-Imaz, A., Simón, J.L., Izquierdo-Llavall, E., Aldega, L., Román Berdiel, T., Osácar, M.C., Pueyo-Anchuela Ansón, M., García-Lasanta, C., Corrado, S., Invernizzi, C., Caricchi, C., 2018. Strain indicators and magnetic fabric in intraplate fault zones: Case study of Daroca thrust, Iberian Chain, Spain. Tectonophysics 730, 29–47. https://doi.org/10.1016/j.tecto.2018.02.013.

Cifelli, F., Mattei, M., Hirt, A.M., Günther, A., 2004. The origin of tectonic fabrics in “undeformed” clays: the early stages of deformation in extensional sedimentary basins. Geophys. Res. Lett. 31, 2–5. https://doi.org/10.1029/2004GL019609.

Cifelli, F., Mattei, M., Chadima, M., Hirt, A.M., Hansen, A., 2005. The origin of tectonic lineation in extensional basins: combined neutron texture and magnetic analyses on “undeformed” clays. Earth Planet. Sci. Lett. 235, 62–78. https://doi.org/10.1016/j. epsl.2005.02.042.

Coianiz, L., Schattner, U., Lang, G., Ben-Avraham, Z., 2019. Between plate and salt tectonics-New stratigraphic constraints on the architecture and timing of the Dead Sea basin during the Late Quaternary. Basin Res. https://doi.org/10.1111/

Elhanati, D., Levi, T., Marco, S., Weinberger, R. 2020. Zones of inelastic deformation around surface ruptures detected by magnetic fabrics. Tectonophysics, 788, 228502.

Ebert, Y., Shaar, R., Levy, E. J., Zhao, X., Roberts, A. P., Stein, M. 2020. Magnetic properties of late Holocene Dead Sea sediments as a monitor of regional hydroclimate. Geochem. Geophys. Geosyst., 21(11), e2020GC009176.

Frank, U., Nowaczyk, N. R., & Negendank, J. F., 2007. Palaeomagnetism of greigite bearing sediments from the Dead Sea, Israel. Geophysical Journal International, 168(3), 904-920.

Fossen, H. 2016. Structural Geology, 463 pp., Cambridge Univ. Press, Cambridge.

Garfunkel, Z. 1981. Internal structure of the Dead Sea leaky transform (rift) in relation to plate kinematics, Tectonophysics, 80(1–4), 81–108.

Hooyer, T. S., Iverson, N. R., Lagroix, F., Thomason, J. F. 2008. Magnetic fabric of sheared till: A strain indicator for evaluating the bed deformation model of glacier flow. J. Geophys. Res.: Earth Surface, 113(F2).

Hrouda, F., 1978. The magnetic fabric in some folds. Physics of the Earth and Planetary Interiors, 17(2), 89-97.

Hrouda, F. 1982. Magnetic anisotropy of rocks and its application in geology and geophysics, Geophys. Surv., 5(1), 37–82.

Hrouda, F., 1993. Theoretical models of magnetic anisotropy to strain relationship revisited. Physics of the Earth and Planetary Interiors, 77, 237-249.Hudleston, P.J. 1986. Extracting information from folds in rocks. Journal of Geological Education, 34, 237–245.

Huddleston, P.J., Treagus, S.H. 2010. Information from folds: A review. Journal of Structural Geology 32, 2042-2071.

Issachar, R., Levi, T., Marco, S., Weinberger, R., 2019a. Strain field associated with a component of divergent motion along the southern Dead Sea fault: Insights from magnetic fabrics. Tectonics, 38(1), 335-353.

Issachar, R., Weinberger, R., Alsop, G. I., Levi, T., 2019b. Deformation of intrasalt beds recorded by magnetic fabrics. J. Geophys. Res.:Solid Earth, 124(12), 12465-12483.

Jelínek, V., 1981. Characterization of the magnetic fabric of rocks. Tectonophysics 79, 63–67.

Kagan, E., Stein, M., Agnon, A., Neumann, F., 2011. Intrabasin paleoearthquake and quiescence correlation of the late Holocene Dead Sea. J. Geophys. Res. 116, B04311.

Ken-Tor, R., Agnon, A., Enzel, Y., Stein, M., Marco, S., Negendank, F.W., 2001. High resolution geological record of historic earthquakes in the Dead Sea basin. J. Geophys. Res. 106, 2221–2234.

Levi, T., Weinberger, R., Aïfa, T. Eyal, Y., Marco, S., 2006a. Injection mechanism of clay-rich sediments into dikes during earthquakes, Geochem. Geophys. Geosyst., 7, Q12009, doi:10.1029/2006GC001410.

Levi, T., Weinberger, R., Aïfa, T. Eyal, Y., Marco, S., 2006b. Earthquake-induced clastic dikes detected by anisotropy of magnetic susceptibility, Geology, 34(2), 69–72.

Levi, T., Weinberger, R. 2011. Magnetic fabrics of diamagnetic rocks and the strain field associated with the Dead Sea Fault, northern Israel. Journal of Structural Geology, 33(4), 566-578.

Levi, T., Weinberger, R., Marco, S., 2014. Magnetic fabrics induced by dynamic faulting reveal damage zone sizes in soft rocks, Dead Sea basin, Geophys. J. Int., 199(2), 1214–1229.

Levi, T., Weinberger, R., Alsop, G.I., Marco, S., 2018. Characterizing seismites with anisotropy of magnetic susceptibility. Geology 46, 827–830. https://doi.org/10.1130/G45120.1

Lisle, R. J. 1992. Strain estimation from flattened buckle folds. J. Struct. Geol., 14(3), 369-371.

Liu, B., Saito, Y., Yamazaki, T., Abdeldayem, A., Oda, H., Hori, K., Zhao, Q. 2001. Paleocurrent analysis for the Late Pleistocene–Holocene incised-valley fill of the Yangtze delta, China by using anisotropy of magnetic susceptibility data. Marine Geology, 176(1-4), 175-189.

Lu, Y., Waldmann, N., Alsop, G.I., Marco, S., 2017. Interpreting soft sediment deformation and mass transport deposits as seismites in the Dead Sea depocentre. J. Geophys. Res.: Solid Earth 122 (10), 8305–8325.

Maltman, A. 1984. On the term "soft-sediment deformation". J. Struct. Geol., 6(5), 589-592.

Mamtani, M. A., Abhijith, V., Lahiri, S., Rana, V., Bhatt, S., Goswami, S., Renjith, A. R., 2017. Determining the reference frame for kinematic analysis in S-tectonites using AMS. Journal of the Geological Society of India, 90(1), 5-8.

Mamtani, M. A., Pal, T., Greiling, R. O., 2013. Kinematic analysis using AMS data from a deformed granitoid. Journal of Structural Geology, 50, 119-132.

Mattei, M., Sagnotti, L., Faccenna, C., Funiciello, R., 1997. Magnetic fabric of weakly deformed clay-rich sediments in the Italian peninsula: relationship with compressional and extensional tectonics. Tectonophysics, 271(1-2), 107-122.

Mattei, M., Speranza, F., Argentieri, A., Rossetti, F., Sagnotti, L., Funiciello, R., 1999. Extensional tectonics in the Amatea basin (Calabria, Italy): a comparison between structural and magnetic anisotropy data. Tectonophysics 307, 33–49.

Mukherji, A., Chaudhuri, A. K., Mamtani, M. A., 2004. Regional scale strain variations in Banded Iron Formations of eastern India: results from anisotropy of magnetic susceptibility studies. Journal of Structural Geology, 26, 2175-2189.

Parés, J.M., Van Der Pluijm, B.A., Dinarès-Turell, J., 1999. Evolution of magnetic fabric during incipient deformation of mudrock (Pyrenees, northen Spain). Tectonophysics 307, 1–14.

Parés, J.M., 2015. Sixty years of anisotropy of magnetic susceptibility in deformed sedimentary rocks, Front. Earth Sci., 3, 4.

Quennell, A. M., 1956. Tectonics of the Dead Sea Rift, in Proceedings Congreso Geologico Internacional, 20th Sesión, pp. 385–405, Asociación de Servicios Geologicos Africanos, Mexico City.

Ramsay, J. G., 1967. Folding and fracturing of rocks. Mc Graw Hill Book Company, 568.

Ramsay, J. G., Huber, M. I., 1983. The techniques of modern structural geology: Strain analysis (Vol. 1). Academic press.

Ramsay, J. G., Huber, M. I., 1987. The techniques of modern structural geology: Folds and fractures (Vol. 2). Academic press.

Ramsay, J. G., Lisle, R. J., 2000. Applications of continuum mechanics in structural geology (Techniques of modern structural geology. Vol. 3). Academic Press.

Rees, A. I., 1966. The effects of depositional slopes on the anisotropy ofmagnetic susceptibility of laboratory deposited sands, J. Geol., 74, 856–867.

Rees, A. I., 1971. The magnetic fabric of a sedimentary rock deposited on a slope. J. Sediment. Res. 41, 307–309.

Rees, A. I., Woodall, W. A., 1975. The magnetic fabric of some laboratory-deposited sediments. Earth Planet. Sci. Lett. https://doi.org/10.1016/0012-821X(75)90188-0.

Rees, A. I. 1983. Experiments on the production of transverse grain alignment in a sheared dispersion. Sedimentology, 30(3), 437-448.

Raposo, M. I. B., Esteves, M. C., dos Santos, P. R. 2021. Can magnetic fabric indicate the direction of a glacier movement? An example from Itararé Group and Aquidauana Formation, Paraná Basin, Brazil. Journal of South American Earth Sciences, 106, 103003.

Ron, H., Nowaczyk, N. R., Frank, U., Marco, S., McWilliams, M. O., 2006. Magnetic properties of Lake Lisan and Holocene Dead Sea sediments and the fidelity of chemical and detrital remanent magnetization. New frontiers in Dead Sea paleoenvironmental research, 401, 171.

Schmalholz, S.M., Podladchikov, Y.Y. 2001. Strain and competence contrast estimation from fold shape. Tectonophysics 340, 195-213.

Schöfisch, T., Koyi, H., Almqvist, B. 2021. Influence of décollement friction on anisotropy of magnetic susceptibility in a fold-and-thrust belt model. Journal of Structural Geology, 144, 104274.

Sneh, A., 1979. Late Pleistocene fan-deltas along the Dead Sea rift. Journal of Sedimentary Research, 49(2), 541-551.

Sen, K., Mamtani, M. A., 2006. Magnetic fabric, shape preferred orientation and regional strain in granitic rocks. Journal of Structural Geology, 28(10), 1870-1882.

Sneh, A., Weinberger, R., 2014. Major Structures of Israel and Environs, Scale 1:500,000: Jerusalem, Israel Geological Survey.

Sneh, A., Rosensaft, M., 2020. Geological Map of Israel. (scale 1:200,000: Jerusalem, Israel Geological Survey).

Soto, R., Larrasoaña, J.C., Arlegui, L.E., Beamud, E., Oliva-Urcia, B., Simón, J.L., 2009. Reliability of magnetic fabric of weakly deformed mudrocks as a palaeostress indicator in compressive settings. J. Struct. Geol. 31, 512–522. https://doi.org/10. 1016/j.jsg.2009.03.006.

Tarling, D., Hrouda, F. (Eds.), 1993. Magnetic anisotropy of rocks. Springer Science and Business Media.

Weinberger, R., Levi, T. Alsop, G. I. Eyal, Y., 2016. Coseismic horizontal slip revealed by sheared clastic dikes in the Dead Sea basin, Geol. Soc. Am. Bull., 128(7–8), 1193–1206.

Weinberger, R., Levi, T., Alsop, G.I., Marco, S., 2017. Kinematics of Mass Transport Deposits revealed by magnetic fabrics. Geophys. Res. Lett. 5807–5817. https://doi. org/10.1002/2017GL072584.

Yechieli, Y., Magaritz, M., Levy, Y., Weber, U., Kafri, U., Woelfli, W., Bonnani, G., 1993. Revision of late quaternary geological history of the Dead Sea area, Israel. Quart. Res. 39, 59–67.

Figure captions

Figure 1: (a) General map showing tectonic plates in the Middle East and the location of the Dead Sea Fault (DSF), a sinistral transform between Sinai subplate and Arabian plate. Red box marks the study area in the Dead Sea basin. Black arrows show the relative plate motion. (b) Generalised map showing the present Dead Sea, including the position of the study site in Ze'elim gully. The extent of the late Pleistocene Lisan Formation and the Holocene Ze'elim Formation and the anthropogenic evaporites of the Dead Sea Ponds are shown. Black box marks the study area. Fault traces are based on Sneh and Weinberger (2014). (c) Oblique drone photograph looking NNW along the previous (yellow dotted lines) and current shorelines of the Dead Sea, highlighting the study site in Ze'elim gully (box marked by a white arrow) and the position of the shoreline separating different slope angles. Rectangle marks the study area of Alsop and Weinberger (2020). The escarpment of the Dead Sea western border fault zone is seen in the background.

Figure 2: (a) Line drawing of the studied folded layer and the associated basal and upper detachments. The studied fold train comprising nine folds are denoted by F_1, F_2,…and F_9. Top-right: lower hemisphere, equal-area projection of hinge orientations (n=7) measured along the studied folded layer. Kamb contouring is with contour interval of 3 sigma, counting area of 12.5% net area and significance level of 1 sigma. Blue arrows indicate the trend of the studied Ze'elim gully. (b) Photograph and annotation (white line) showing the sampled folded layer and the basal detachment in the Ze'elim gully. Location of samples and their serial numbers are denoted. Basal detachment - 1-19 (red); folded layers – 20-77 (yellow); toe of fold – 78-87 (green).

Figure 3: (a) - (i) Photographs and detailed line drawings of F_1 to F_9 folds, including traces of axial planes (thick white line) and representative dip isogons (thin white lines). c), j), k), l) Charts of dip-isogon analyses based on Ramsay (1967, see text) with data separated into backlimb and forelimb of each fold.

Figure 4: Application of the inverse-thickness method (Lisle, 1992; see text) to the studied folded layer, showing flattening strain ellipses for the F_1 to F_9 folds. The inverse thickness method plots (1/*t*) for various orientations of the layer tangent around the fold, where *t* is the orthogonal thickness (see Lisle 1992, p.370). The inverse thickness (1/*t*) is plotted from a common central point, each in the direction of the tangent to create an array of points to which a best-fit ellipse is matched. *Rs* value is the ratio of the ellipse long to short axes.

Figure 5: Graphs comparing parameters measured from the folded layer. (a) Fold amplitude (*A*) versus wavelength (λ), (b) fold amplitude / wavelength plotted against wavelength, (c) Strain contour maps of Schmalholz and Podladchikov (2001) that plot fold amplitude / wavelength against layer thickness / wavelength. The grid lines show estimated % shortening and viscosity contrasts for folded layers. Arrow highlights the gentle slope of the data compared to viscosity contrast lines on the map. (d) Elliptical ratio (*Rs*) of Lisle (1992) plotted against the forelimb / axial plane ratio (R_{FAP}). *T* parameter from AMS analysis is plotted against (e) the forelimb to backlimb thickness ratio (R_{FB}), and (f) the forelimb to axial-plane thickness ratio (R_{FAP}). Arrows show general trends of data on each graph, while F_1 – F_9 labels correspond to individual folds. In (b) and (c) syncline hinges are distinguished by the blue squares.

Figure 6: (a) Frequencies of mean susceptibilities (K_{m}) of 97 studied samples. (b) *T* versus K_m diagram; (c) *P* versus K_m diagram.

Figure 7: Cartoon schematically illustrating a folded layer and distributed AMS data that are grouped into structural domains, including a basal detachment, backlimbs, forelimbs, anticline and syncline hinge zones, and toe of the slump as well as data from an 'undeformed' reference layer. Stereoplots are lower hemisphere, equal-area projection of AMS principal axes (eigenvectors) with 95% confidence ellipses. Red squares, green triangles, and blue circles represent the K_1, K_2, and K_3 axes, respectively. T-P diagrams show the shape T versus the degree of anisotropy P of the AMS eigenvalues. Flow direction is marked by a black arrow and movement direction along the basal detachment by green arrows. HZ-hinge zone; AP-axial plane. Top-right: Lower hemisphere, equal-area projection of hinge-line orientations (n=7) measured along the studied folded layer (see also inset in Fig. 2a). Note that the hinge lines are sub-parallel to the K_1 axes in anticline and syncline hinge zones.

Figure 8: AMS data of the studied folded layer, basal detachment zone, and the 'undeformed' reference layer in Ze'elim gully plotted in (a) Flinn-type diagram (i.e., magnetic lineation versus magnetic foliation), where line of neutral shape separates prolate and oblate shapes of the AMS ellipsoid; and (b) T-ln(L) diagram (Levi et al., 2018), where T is the shape of the AMS ellipsoid and L is the magnetic lineation. $T>0$ represents an oblate shape; $T<0$ represents a prolate shape and $T=0$ is attributed to a neutral shape. Dashed lines radiating from $T=1$ (pure oblate) are lines of equal k_1/k_3 ratios (i.e., eccentricity P of the AMS ellipsoids), which are fitted to sub-sets of the AMS data according to their structural domains (backlimbs, forelimbs, anticline and syncline hinges; R^2 are indicated). Line characterizing the 'deposition environment' is fitted to data from the 'undeformed' reference layer; line characterizing the 'detachment process' is fitted to data from the detachment; and a line corresponding to the 'folding process' is fitted to the data from fold domains including the backlimbs, forelimbs and hinge zones. Data from the toe of the slump are not presented. Legend for (a) and (b) is the same.

Figure 9: Variations of (a) *T*, the shape of the AMS ellipsoid, and (b) K_m the magnetic susceptibility, along the studied folded layer and its toe, denoted by serial numbers between 20 (west) and 87 (east). Vertical dotted lines mark the boundaries between two adjacent folds (e.g., F_1 and F_2). Values from different structural domains (backlimb, forelimb, anticline and syncline hinge zones) are marked with different symbols (see legend). Dashed red arrows highlight decreasing values of *T* from backlimbs to anticline hinge zones, and blue dashed arrows highlight the increasing value of *T* from local minima in syncline hinge zones to backlimbs.

Figure 10: GIS-based maps showing the interpolated spatial distribution of the AMS parameters within the folded layer for (a) *L*, (b) *F*, (c) *P*, and (d) *T*. The diameter and location of circles correspond to the extracted AMS specimens and their measured values are related to the colour scale to the left. Fold structures F_1, F_2,…F_9 are labelled.

Figure 11: GIS-based maps showing the interpolated spatial distribution of calculated (a) *L*/*F* ratios, and(b) *T*/*L* ratios. (c) R_{FAP} values in coloured circles in a scale between 0.27 and 0.95 on top of the spatial distribution of *T* within the folded layer. Fold structures F_1, F_2,…F_9 are marked. (d) *Rs* values presented in coloured circles in a scale between 1.92 and 4.08 on top of the spatial distribution of *T* within the folded layer. (e) *Rs* values presented in coloured circles in a scale between 1.92 and 4.08 on top of the spatial distribution of *P* within the folded layer.

Figure 12: Summary cartoon illustrating a folded layer formed along an inclined basal detachment (slope $>5^{o}$). Different structural domains, including the backlimb, forelimb, hinge zone (HZ), and the toe of the slump are marked. The downslope flow is marked by a black arrow, while the movement direction along the basal detachment is indicated by green arrows. Small block diagrams show sections through the AMS ellipsoid while adjacent Flinn-

type diagrams schematically display the plotted AMS data for the different structural domains. The blue diagonal lines on the Flinn-type diagrams correspond to plane strain, while *L* and *F* labels refer to lineation and foliation respectively. The ellipsoids on the block diagrams are orientated such that the maximum AMS axis is parallel to the fold hinges. For comparison, the AMS ellipsoid from an ‘undeformed’ reference layer is shown on the left.

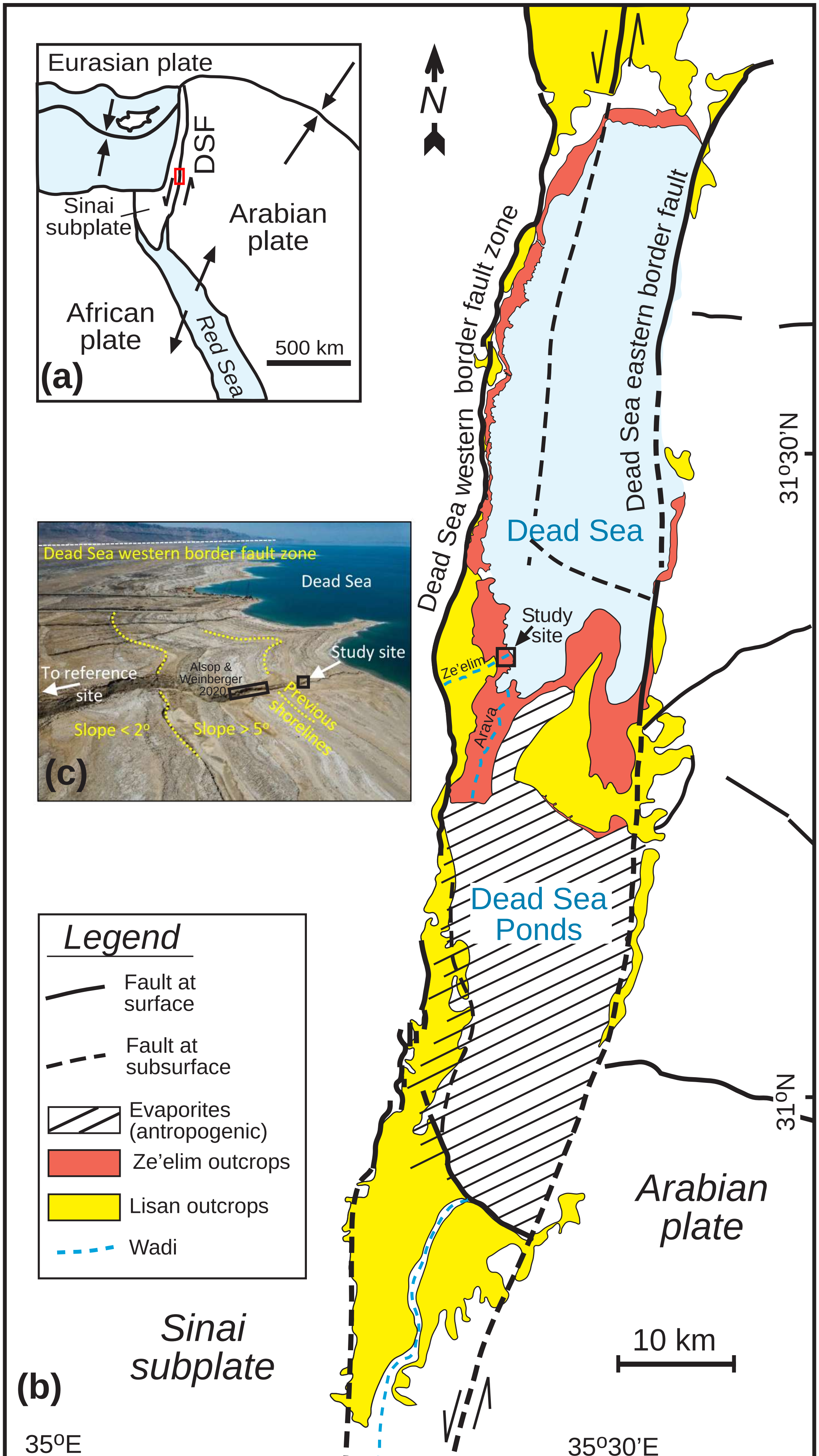
Eurasian plate
DSF
Sinai
subplate
Arabian
plate
African
plate
Red Sea
500 km
(a)
Dead Sea western border fault zone
Dead Sea
To reference
site
Alsop &
Weinberger
2020
Study site
Previous
shorelines
Slope < 2°
Slope > 5°
(c)
N
Dead Sea western border fault zone
Dead Sea eastern border fault
31°30'N
Dead Sea
Study
site
Ze'elim
Arava
Dead Sea
Ponds
Legend
Fault at
surface
Fault at
subsurface
Evaporites
(antropogenic)
Ze'elim outcrops
Lisan outcrops
Wadi
31°N
Arabian
plate
Sinai
subplate
10 km
(b)
35°E
35°30'E

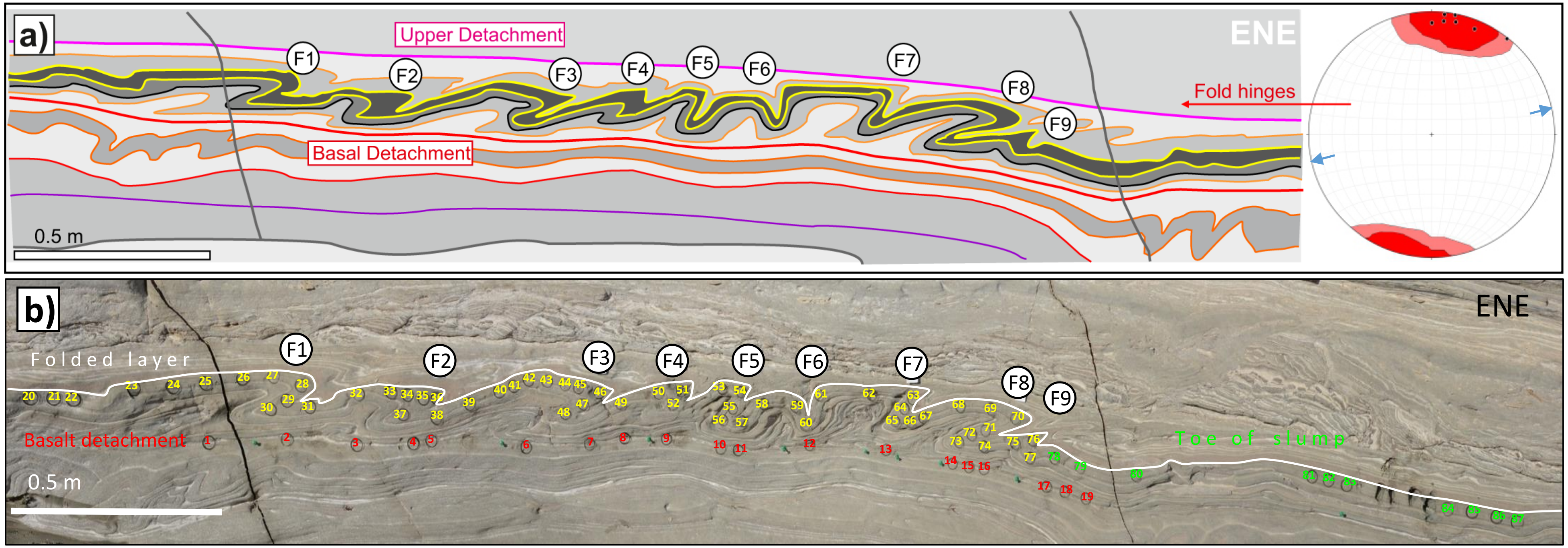
a)
Upper Detachment
F1
F2
F3
F4
F5
F6
F7
F8
F9
ENE
Fold hinges
Basal Detachment
0.5 m
b)
ENE
Folded layer
Basalt detachment
Toe of slump
0.5 m

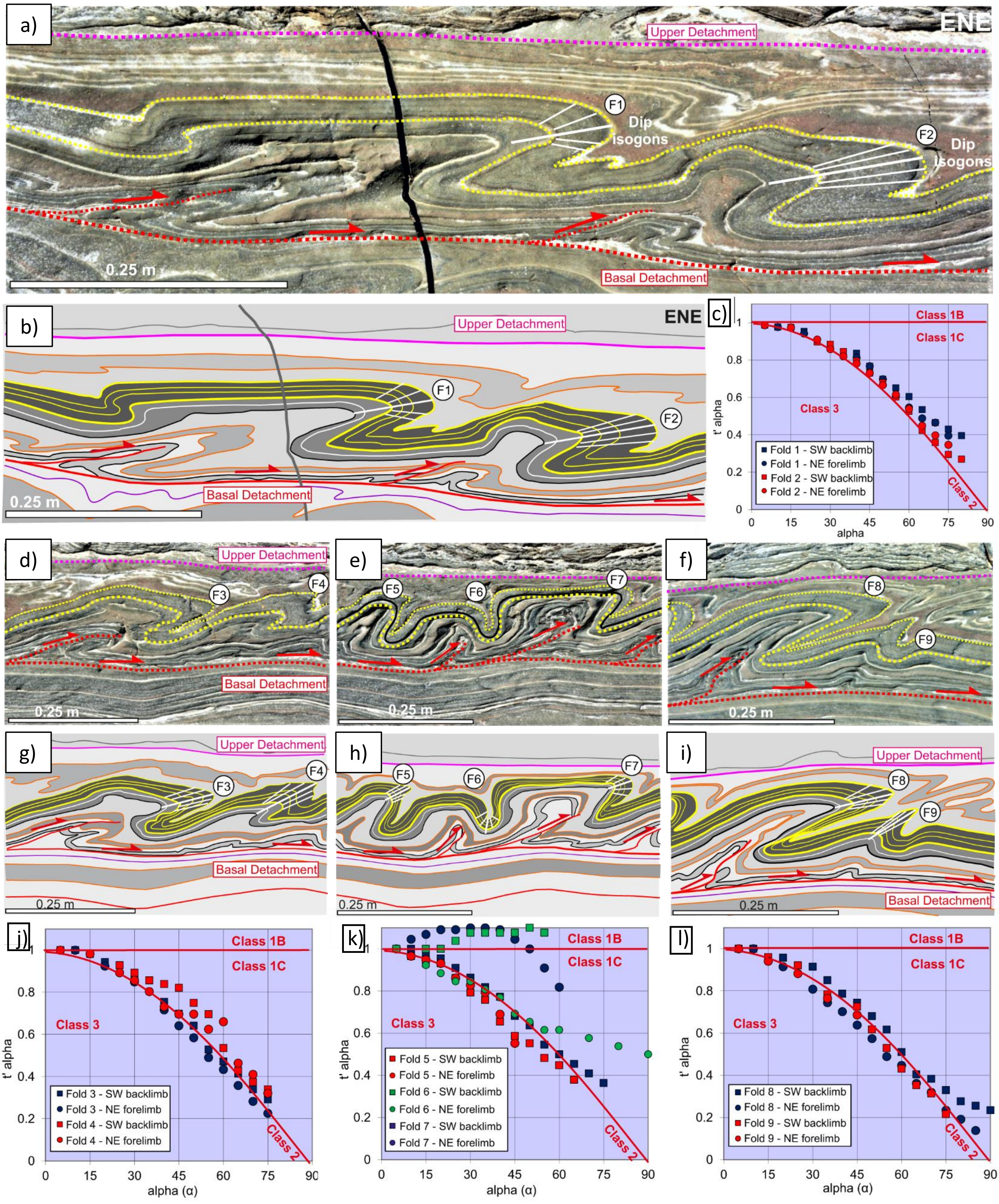

a)
ENE
Upper Detachment
F1
Dip isogons
F2
Dip isogons
0.25 m
Basal Detachment
b)
ENE
Upper Detachment
F1
F2
0.25 m
Basal Detachment
c)
Class 1B
Class 1C
Class 3
Class 2
t' alpha
alpha
Fold 1 - SW backlimb
Fold 1 - NE forelimb
Fold 2 - SW backlimb
Fold 2 - NE forelimb
d)
Upper Detachment
F3
F4
Basal Detachment
0.25 m
e)
F5
F6
F7
0.25 m
f)
F8
F9
0.25 m
g)
Upper Detachment
F3
F4
Basal Detachment
0.25 m
h)
F5
F6
F7
0.25 m
i)
Upper Detachment
F8
F9
0.25 m
Basal Detachment
j)
Class 1B
Class 1C
Class 3
Class 2
t' alpha
alpha (α)
Fold 3 - SW backlimb
Fold 3 - NE forelimb
Fold 4 - SW backlimb
Fold 4 - NE forelimb
k)
Class 1B
Class 1C
Class 3
Class 2
t' alpha
alpha (α)
Fold 5 - SW backlimb
Fold 5 - NE forelimb
Fold 6 - SW backlimb
Fold 6 - NE forelimb
Fold 7 - SW backlimb
Fold 7 - NE forelimb
l)
Class 1B
Class 1C
Class 3
Class 2
t' alpha
alpha (α)
Fold 8 - SW backlimb
Fold 8 - NE forelimb
Fold 9 - SW backlimb
Fold 9 - NE forelimb

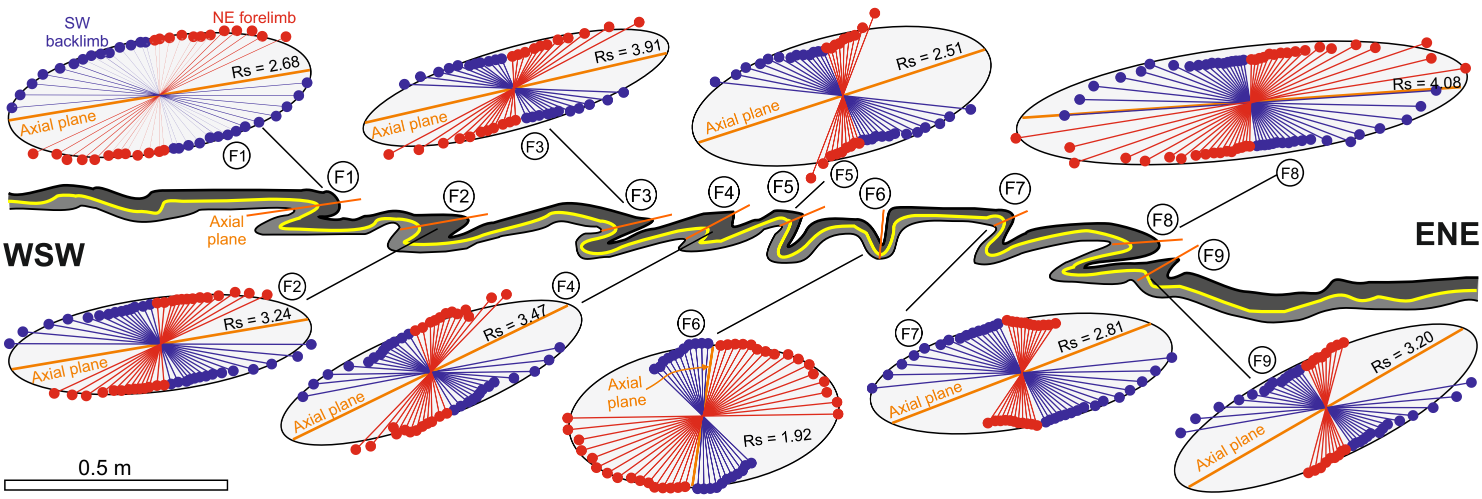

SW backlimb
NE forelimb
Rs = 2.68
Axial plane
F1
Rs = 3.91
F3
Rs = 2.51
F5
Rs = 4.08
F8
Axial plane
F2
F4
F6
F7
F9
WSW
ENE
Rs = 3.24
Rs = 3.47
Rs = 1.92
Rs = 2.81
Rs = 3.20
0.5 m

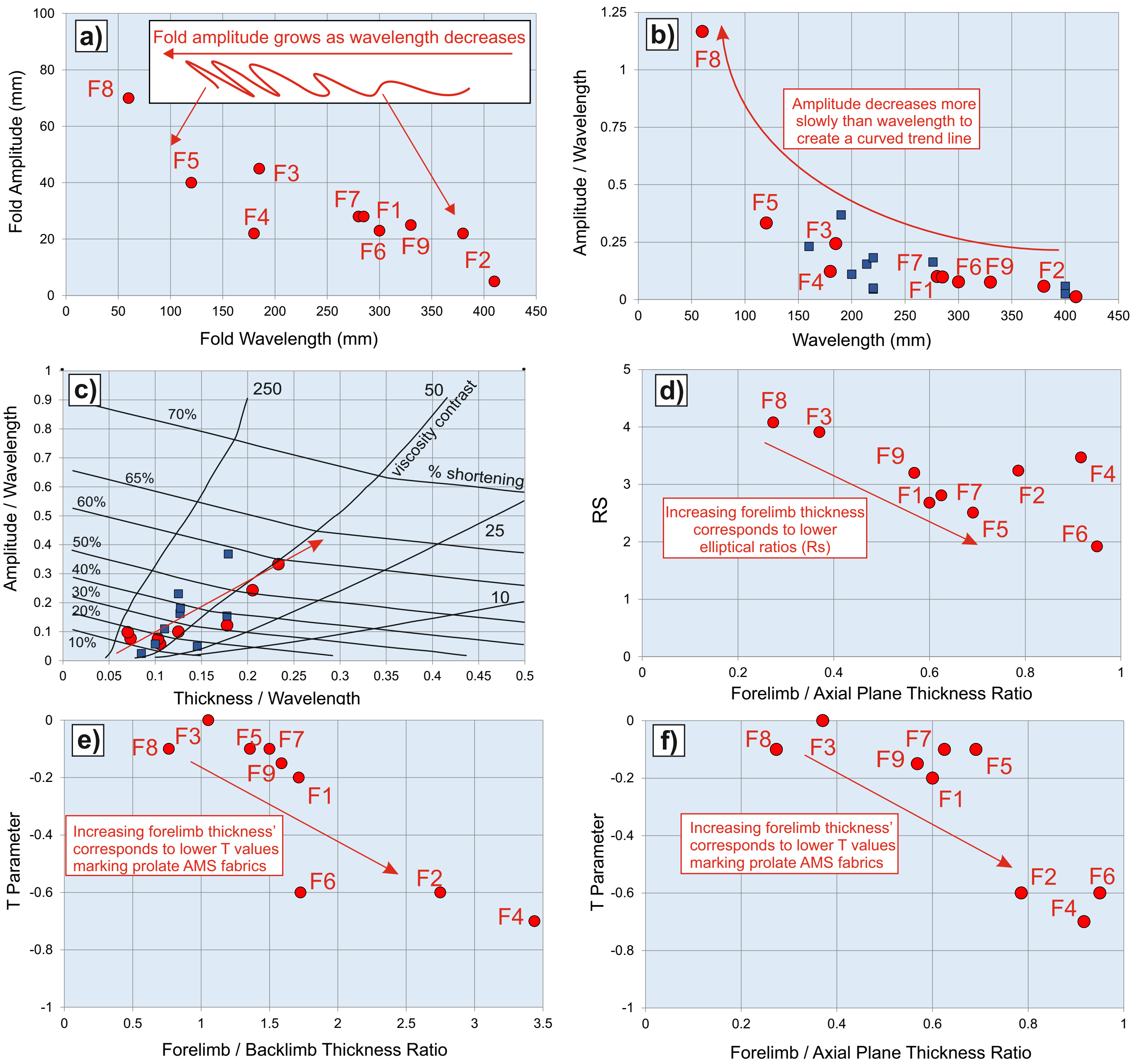
a)
Fold amplitude grows as wavelength decreases
Fold Amplitude (mm)
Fold Wavelength (mm)
F8
F5
F3
F4
F7
F1
F6
F9
F2
b)
Amplitude decreases more slowly than wavelength to create a curved trend line
Amplitude / Wavelength
Wavelength (mm)
c)
Amplitude / Wavelength
Thickness / Wavelength
250
50
25
10
viscosity contrast
% shortening
70%
65%
60%
50%
40%
30%
20%
10%
d)
RS
Increasing forelimb thickness corresponds to lower elliptical ratios (Rs)
Forelimb / Axial Plane Thickness Ratio
e)
T Parameter
Increasing forelimb thickness' corresponds to lower T values marking prolate AMS fabrics
Forelimb / Backlimb Thickness Ratio
f)
T Parameter
Increasing forelimb thickness' corresponds to lower T values marking prolate AMS fabrics
Forelimb / Axial Plane Thickness Ratio

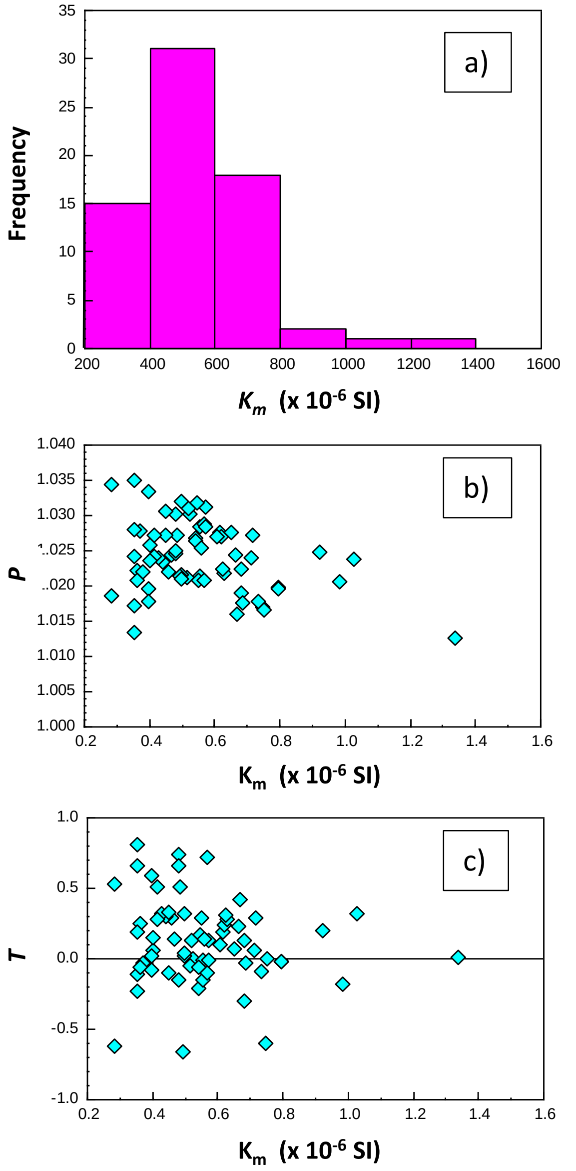

a)
Frequency
K_m (x 10^{-6} SI)
b)
P
K_m (x 10^{-6} SI)
c)
T
K_m (x 10^{-6} SI)

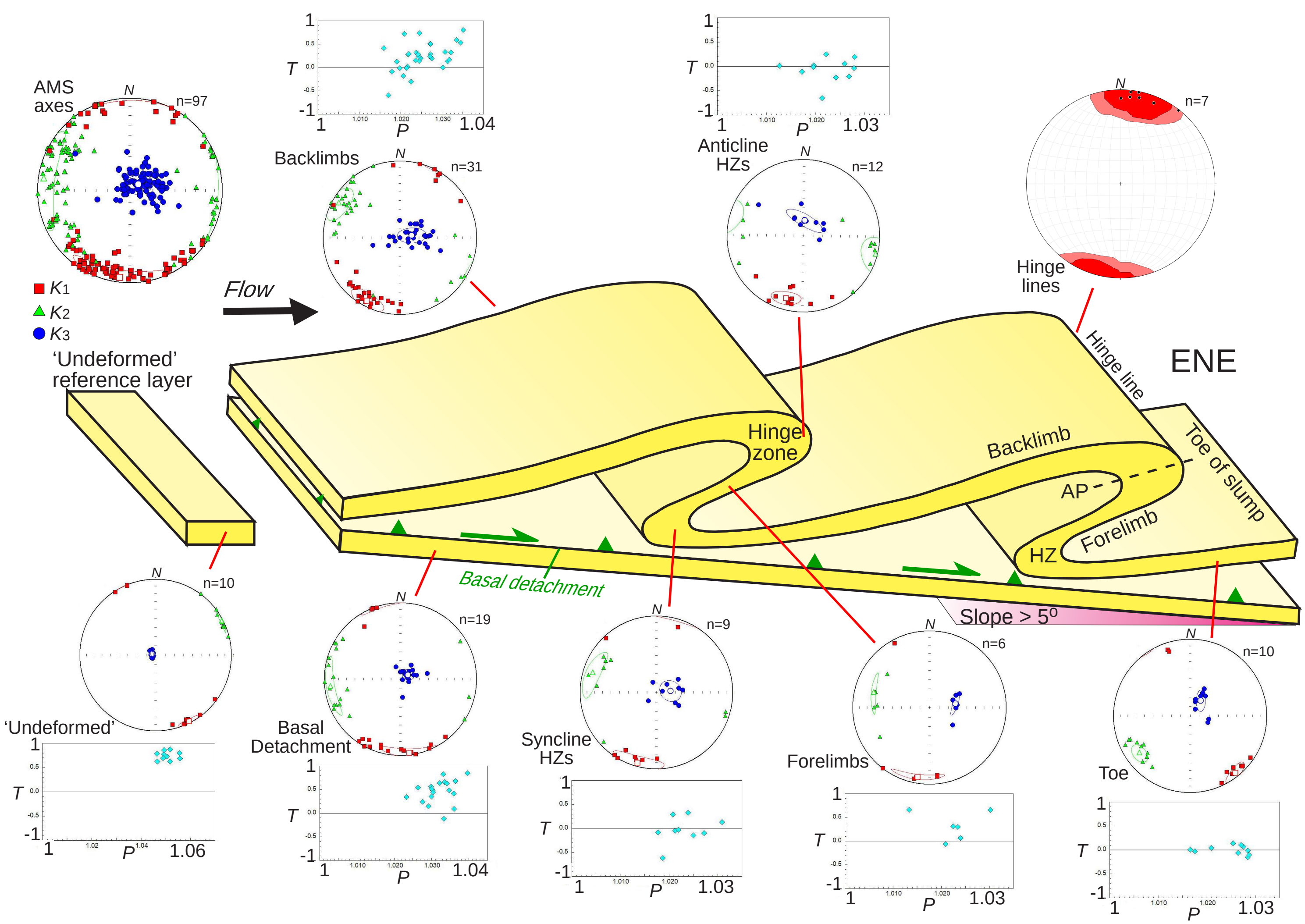

AMS axes
N
n=97
K1
K2
K3
'Undeformed' reference layer
Flow
Backlimbs
n=31
Anticline HZs
n=12
Hinge lines
n=7
ENE
Hinge line
Toe of slump
Hinge zone
Backlimb
AP
Forelimb
HZ
Basal detachment
Slope > 5°
n=10
'Undeformed'
Basal Detachment
n=19
Syncline HZs
n=9
Forelimbs
n=6
Toe
n=10
T
P

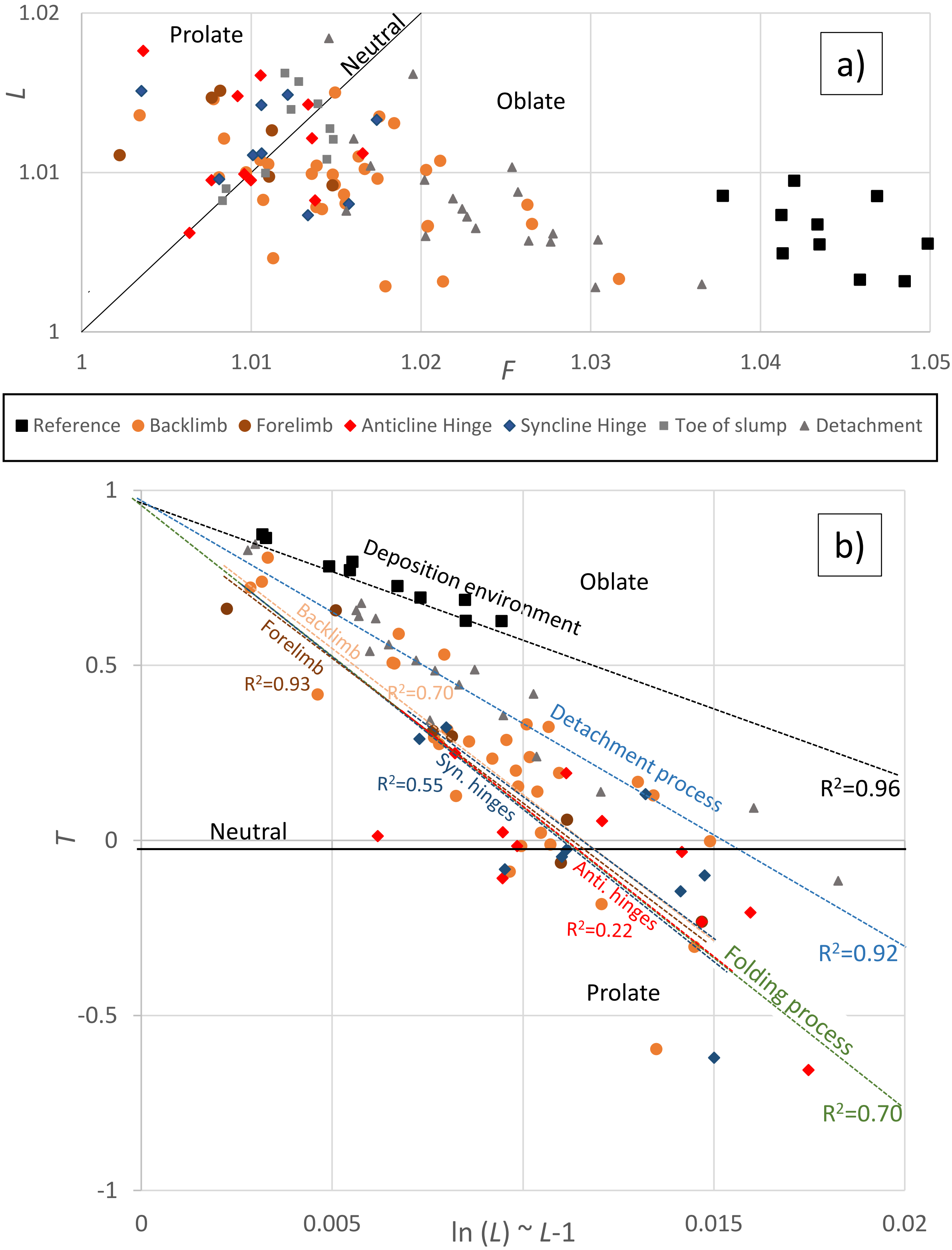

a)
Prolate
Neutral
Oblate
L
F
1.02
1.01
1
1
1.01
1.02
1.03
1.04
1.05
Reference
Backlimb
Forelimb
Anticline Hinge
Syncline Hinge
Toe of slump
Detachment
b)
Deposition environment
Oblate
Backlimb
Forelimb
R2=0.93
R2=0.70
Detachment process
R2=0.96
Syn. hinges
R2=0.55
Neutral
Anti. hinges
R2=0.22
R2=0.92
Folding process
Prolate
R2=0.70
T
1
0.5
0
-0.5
-1
0
0.005
ln (L) ~ L-1
0.015
0.02

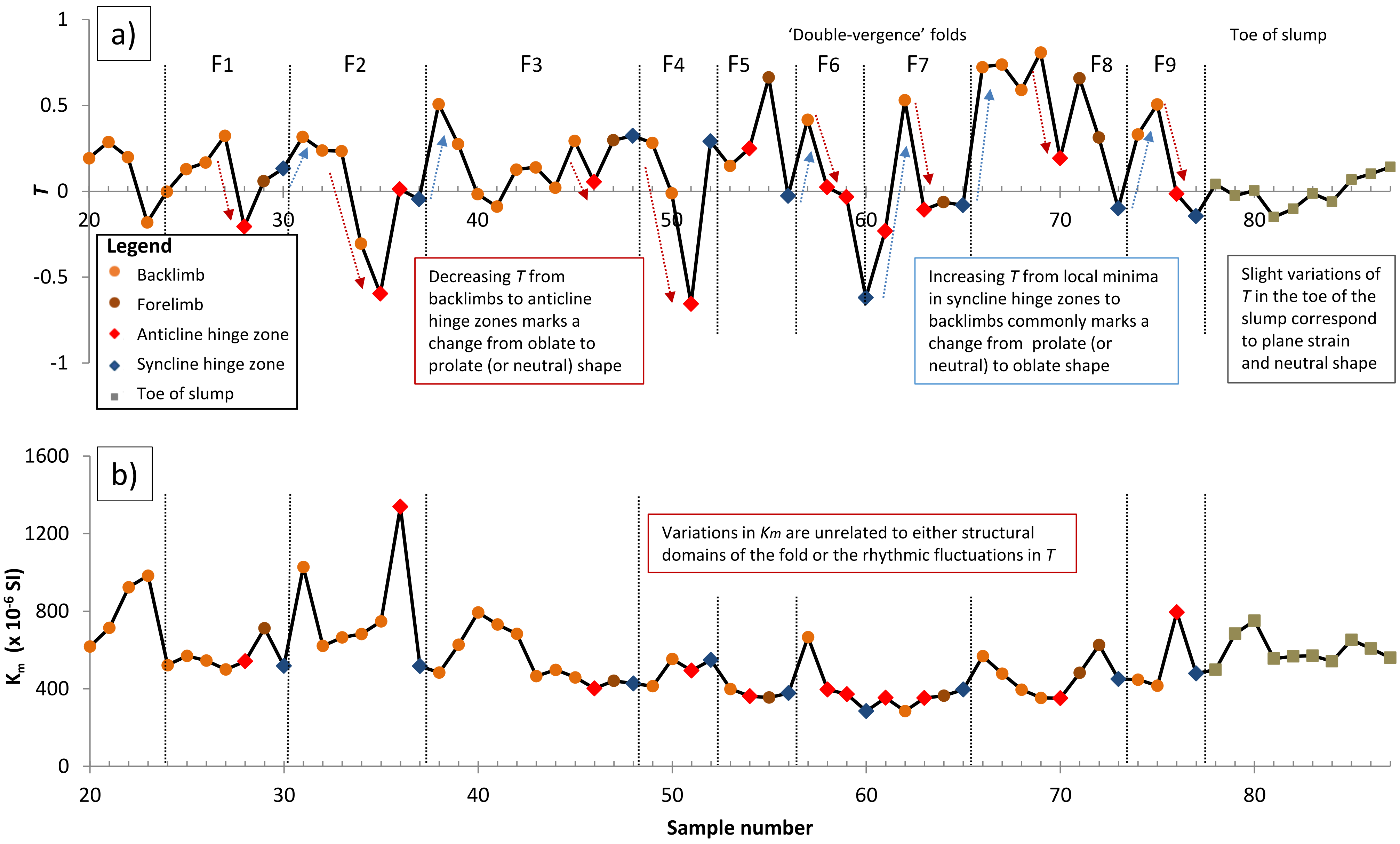
a)
b)
'Double-vergence' folds
Toe of slump
F1
F2
F3
F4
F5
F6
F7
F8
F9
1
0.5
0
-0.5
-1
T
20
30
40
50
60
70
80
Legend
Backlimb
Forelimb
Anticline hinge zone
Syncline hinge zone
Toe of slump
Decreasing T from backlimbs to anticline hinge zones marks a change from oblate to prolate (or neutral) shape
Increasing T from local minima in syncline hinge zones to backlimbs commonly marks a change from prolate (or neutral) to oblate shape
Slight variations of T in the toe of the slump correspond to plane strain and neutral shape
1600
1200
800
400
0
Km (x 10-6 SI)
Variations in Km are unrelated to either structural domains of the fold or the rhythmic fluctuations in T
Sample number

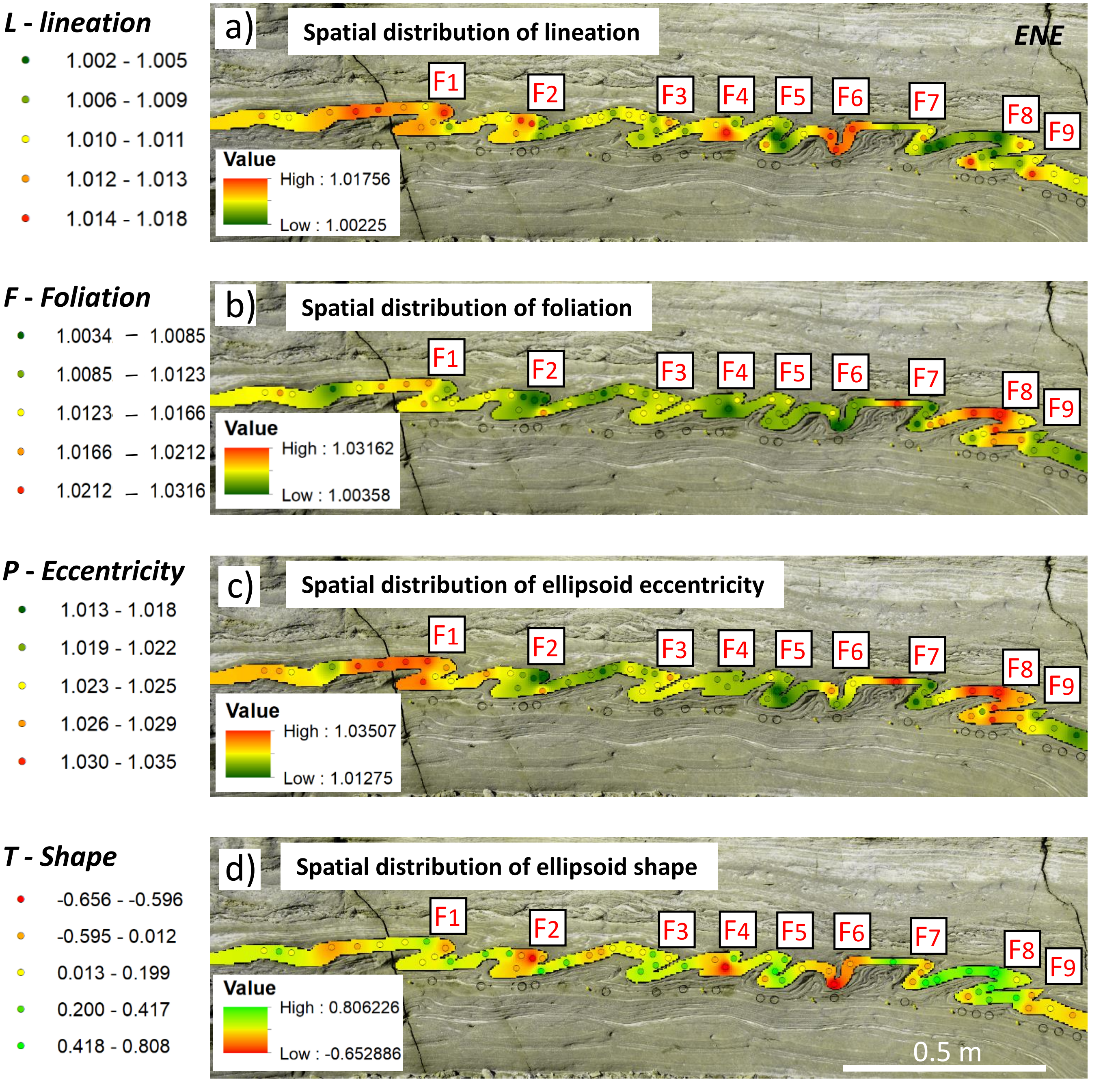

L - lineation
1.002 - 1.005
1.006 - 1.009
1.010 - 1.011
1.012 - 1.013
1.014 - 1.018
a)
Spatial distribution of lineation
ENE
F1
F2
F3
F4
F5
F6
F7
F8
F9
Value
High : 1.01756
Low : 1.00225
F - Foliation
1.0034 – 1.0085
1.0085 – 1.0123
1.0123 – 1.0166
1.0166 – 1.0212
1.0212 – 1.0316
b)
Spatial distribution of foliation
Value
High : 1.03162
Low : 1.00358
P - Eccentricity
1.013 - 1.018
1.019 - 1.022
1.023 - 1.025
1.026 - 1.029
1.030 - 1.035
c)
Spatial distribution of ellipsoid eccentricity
Value
High : 1.03507
Low : 1.01275
T - Shape
-0.656 - -0.596
-0.595 - 0.012
0.013 - 0.199
0.200 - 0.417
0.418 - 0.808
d)
Spatial distribution of ellipsoid shape
Value
High : 0.806226
Low : -0.652886
0.5 m

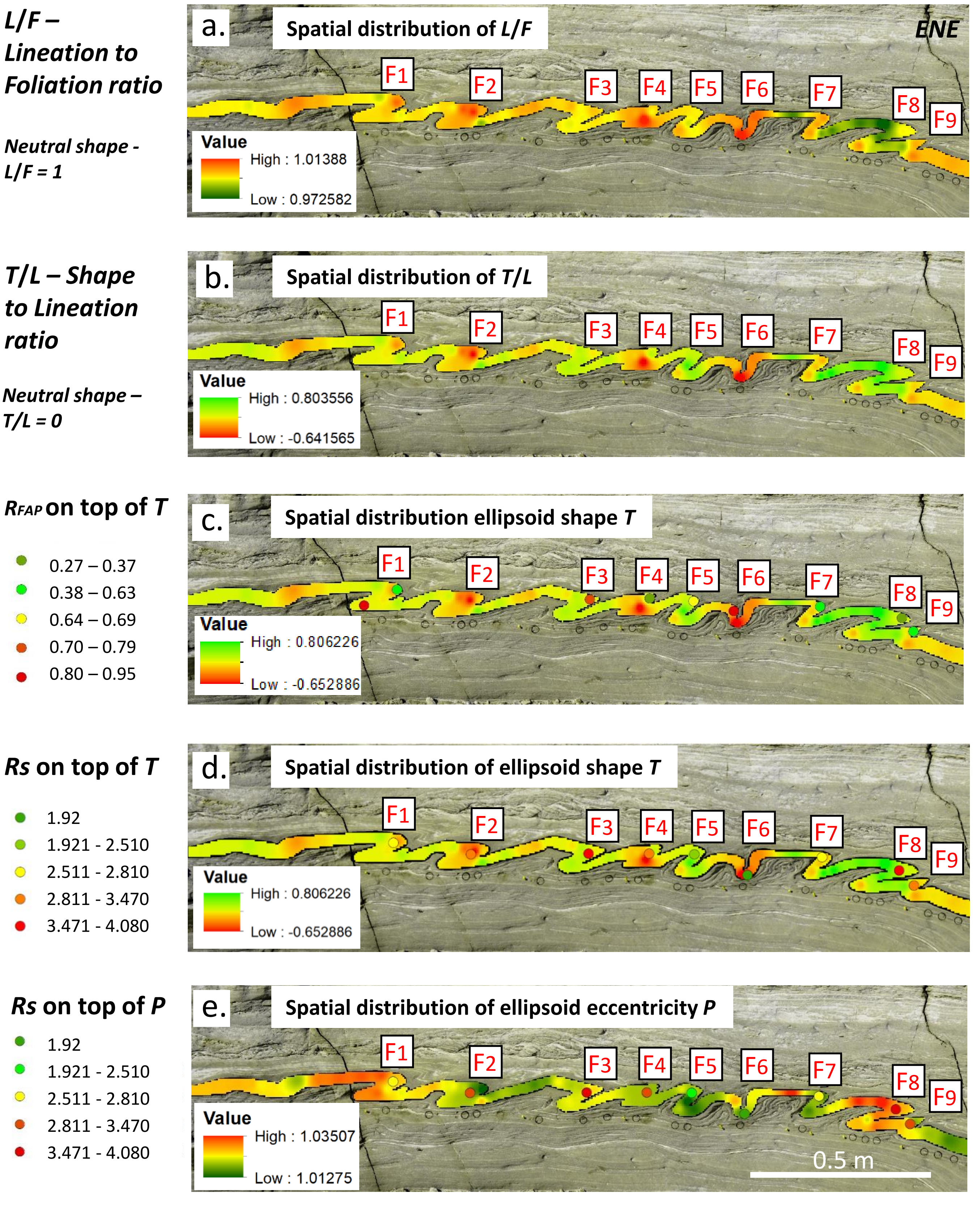

L/F – Lineation to Foliation ratio
Neutral shape - L/F = 1
a.
Spatial distribution of L/F
ENE
F1
F2
F3
F4
F5
F6
F7
F8
F9
Value
High : 1.01388
Low : 0.972582
T/L – Shape to Lineation ratio
Neutral shape – T/L = 0
b.
Spatial distribution of T/L
Value
High : 0.803556
Low : -0.641565
RFAP on top of T
0.27 – 0.37
0.38 – 0.63
0.64 – 0.69
0.70 – 0.79
0.80 – 0.95
c.
Spatial distribution ellipsoid shape T
Value
High : 0.806226
Low : -0.652886
Rs on top of T
1.92
1.921 - 2.510
2.511 - 2.810
2.811 - 3.470
3.471 - 4.080
d.
Spatial distribution of ellipsoid shape T
Value
High : 0.806226
Low : -0.652886
Rs on top of P
1.92
1.921 - 2.510
2.511 - 2.810
2.811 - 3.470
3.471 - 4.080
e.
Spatial distribution of ellipsoid eccentricity P
Value
High : 1.03507
Low : 1.01275
0.5 m

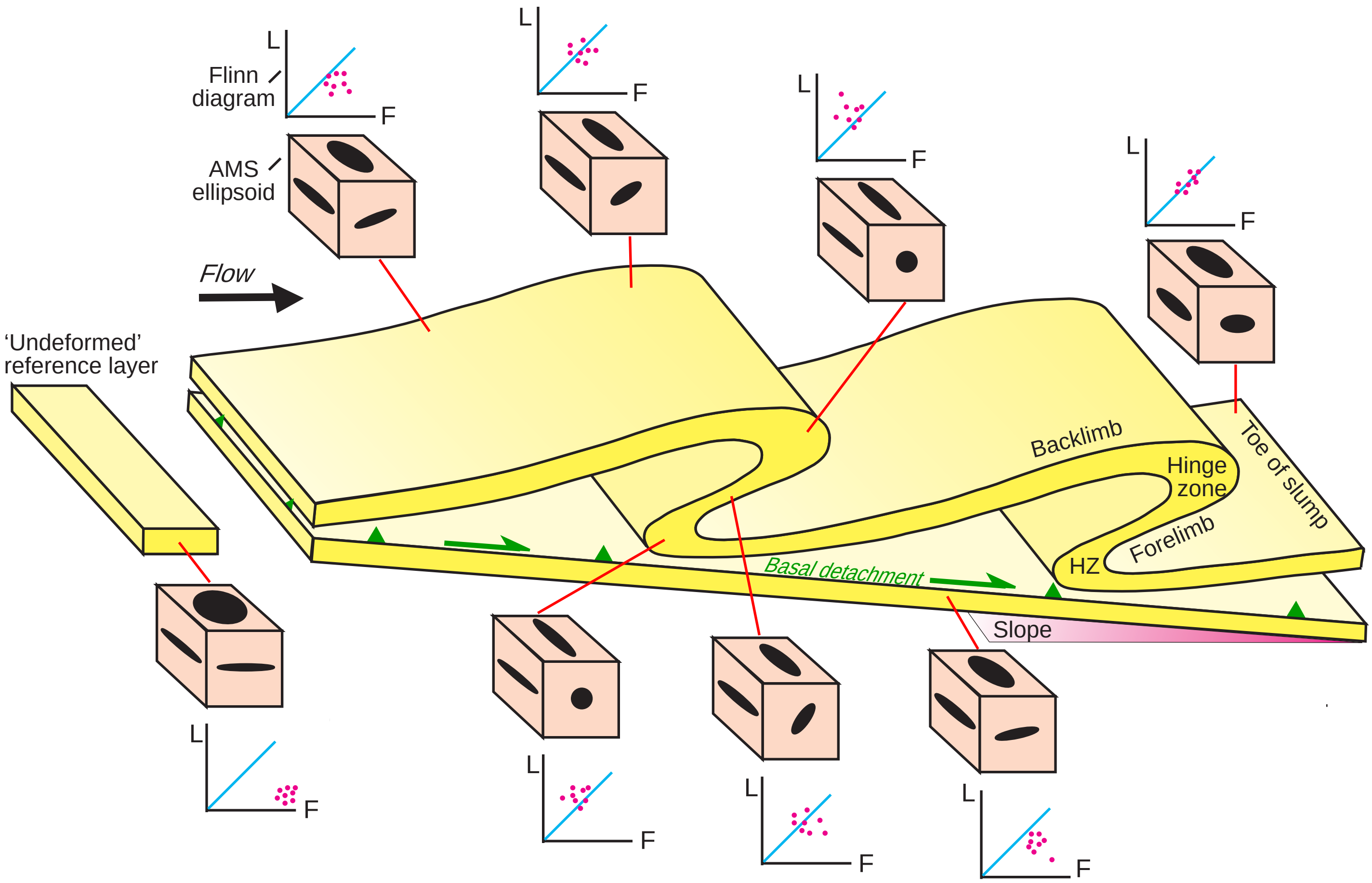

Flinn diagram
AMS ellipsoid
L
F
Flow
'Undeformed' reference layer
Backlimb
Hinge zone
Forelimb
HZ
Toe of slump
Basal detachment
Slope